Article

Colorimetric histology using plasmonically active microscope slides

https://doi.org/10.1038/s41586-021-03835-2

Received: 3 November 2017

Accepted: 19 July 2021

Published online: 6 October 2021

Check for updates

Eugeniu Balaur[1,2], Sandra O'Toole[3,4,5], Alex J. Spurling[6], G. Bruce Mann[7], Belinda Yeo[8,9], Kate Harvey[4], Catherine Sadatnajafi[1,2], Eric Hanssen[10], Jacqueline Orian[11], Keith A. Nugent[1,12], Belinda S. Parker[6,11,13] ✉ & Brian Abbey[1,2] ✉

The human eye can distinguish as many as 10,000 different colours but is far less sensitive to variations in intensity[1], meaning that colour is highly desirable when interpreting images. However, most biological samples are essentially transparent, and nearly invisible when viewed using a standard optical microscope[2]. It is therefore highly desirable to be able to produce coloured images without needing to add any stains or dyes, which can alter the sample properties. Here we demonstrate that colorimetric histology images can be generated using full-sized plasmonically active microscope slides. These slides translate subtle changes in the dielectric constant into striking colour contrast when samples are placed upon them. We demonstrate the biomedical potential of this technique, which we term histoplasmonics, by distinguishing neoplastic cells from normal breast epithelium during the earliest stages of tumorigenesis in the mouse MMTV-PyMT mammary tumour model. We then apply this method to human diagnostic tissue and validate its utility in distinguishing normal epithelium, usual ductal hyperplasia, and early-stage breast cancer (ductal carcinoma in situ). The colorimetric output of the image pixels is compared to conventional histopathology. The results we report here support the hypothesis that histoplasmonics can be used as a novel alternative or adjunct to general staining. The widespread availability of this technique and its incorporation into standard laboratory workflows may prove transformative for applications extending well beyond tissue diagnostics. This work also highlights opportunities for improvements to digital pathology that have yet to be explored.

Plasmonic hole arrays can support specific optical band structures that enable a range of colours to be obtained through precise control of the device geometry[3]. Colour filtering was first achieved using sub-wavelength gratings[4,5] and later via periodic arrays of nanoapertures[6]. The dynamic range of the colour palette for these structures can be extended by incorporating asymmetries in the design and exploiting the specific interactions of polarized light with the local surface plasmon resonances[7,8]. Particularly relevant here are techniques for fabricating these structures over large areas, which are also suitable for low-cost mass production[7,9,10]. Among the approaches that have been tried, directed self-assembly[11], nanoimprint[12], laser interference lithography[10] and displacement Talbot lithography[13] have been suggested as a viable means of mass production. Here, we use displacement Talbot lithography to produce devices on the scale of standard microscope slides (for example, 75 mm × 25 mm) and incorporate them into conventional bright-field imaging of histological tissue sections. We present data from the MMTV-PyMT mouse model with distinct stages of early breast cancer pathology ($N = 6$) and a retrospective patient cohort ($N = 24$) encompassing tissues derived from patients diagnosed with benign usual ductal hyperplasia (UDH) or ductal carcinoma in situ (DCIS), an early stage of breast cancer. Tissues from healthy patients as well as invasive cancers are included as a control. Data are scored by a human breast and murine mammary gland pathologist and the optical output quantified.

Although general histopathology stains such as haematoxylin and eosin (H&E) that allow assessment of tissue morphology are a mainstay of disease diagnostics, identifying abnormal cells, which may be morphologically similar to healthy cells, can be challenging and can

[1]Australian Research Council Centre of Excellence for Advanced Molecular Imaging, La Trobe University, Melbourne, Victoria, Australia. [2]Department of Chemistry and Physics, La Trobe Institute for Molecular Science (LIMS), La Trobe University, Melbourne, Victoria, Australia. [3]Department of Tissue Pathology and Diagnostic Oncology, Royal Prince Alfred Hospital, Camperdown, New South Wales, Australia. [4]The Kinghorn Cancer Centre and Cancer Research Division, Garvan Institute of Medical Research, Darlinghurst, New South Wales, Australia. [5]Sydney Medical School, University of Sydney, Camperdown, New South Wales, Australia. [6]Cancer Immunology Program, Peter MacCallum Cancer Centre, Melbourne, Victoria, Australia. [7]Department of Surgery, The Royal Melbourne Hospital, The University of Melbourne, Parkville, Victoria, Australia. [8]Medical Oncology, Olivia Newton-John Cancer Research Institute, Melbourne, Victoria, Australia. [9]Department of Medical Oncology, Austin Health, Melbourne, Victoria, Australia. [10]Ian Holmes Imaging Center and Department of Biochemistry and Pharmacology, Bio21 Molecular Science and Biotechnology Institute, The University of Melbourne, Parkville, Victoria, Australia. [11]Department of Biochemistry and Genetics, La Trobe Institute for Molecular Science (LIMS), La Trobe University, Melbourne, Victoria, Australia. [12]Research School of Physics, The Australian National University, Acton, Australian Capital Territory, Australia. [13]Sir Peter MacCallum Department of Oncology, The University of Melbourne, Parkville, Victoria, Australia. ✉e-mail: belinda.parker@petermac.org; b.abbey@latrobe.edu.au

lead to discordance between pathologists. Using molecular targets or biomarkers for distinguishing disease states can be labour intensive and time-consuming[14]. Label-free approaches to histology offer a potential alternative or adjunct method of diagnosis that is not reliant on any specific chemical interaction with the sample yet has the potential to detect differences between a normal and a diseased cellular state. These advantages have driven the development of a wide variety of new approaches to histology in recent years, including photoacoustic and ultraviolet microscopy[15,16], quantitative mass spectroscopy and bioanalytical imaging[17], stimulated Raman scattering microscopy[18,19] and quantitative phase imaging[20]. Both photoacoustic and ultraviolet microscopy provide depth resolution[15], but they require specialized equipment and data analysis. Mass spectroscopy is able to quantify protein amounts[17] but it does not yield histology-like images, which can be a critical aid or adjunct to diagnosis. Another label-free technique growing in popularity is stimulated Raman scattering microscopy[18,19]. This technique provides molecular specificity and has been shown to allow for imaging of DNA[16], but it is also time-consuming and therefore may not be suitable for use in surgery or for large samples. Finally, quantitative phase imaging can be used to generate spatially resolved maps of the tissue density[20]. However, this technique does not generate colour-contrast images and may require specialized software and training for data collection. In summary, while each label-free technique has specific advantages and disadvantages for the user, in terms of analysis time, cost, ease of use and compatibility with existing pathology workflows, the technique introduced here, histoplasmonics, offers substantial advantages (see Extended Data Table 1).

Fundamental principles

Extraordinary optical contrast involves the resonant interaction of light with the collective oscillations of free electrons at a metal surface, known as surface plasmon polaritons (SPPs). The spectral change in transmitted light through an array of subwavelength apertures in contact with a thin dielectric specimen (Fig. 1a) is a function of the wavelength shift, $\Delta\lambda$, of the SPP resonant modes. When using a standard transmission bright-field microscope, a spatially resolved distribution of colours will result that relates directly to changes in the local sample thickness and/or dielectric constant. With the local dielectric constant encoded in the optical spectrum, a marked chromatic contrast effect is produced. This potentially means that difficult-to-detect features within an optically transparent sample may be clearly seen in the visible-light transmission image, via plasmon-enhanced colour contrast. This form of colorimetric full-field imaging and its potential applications are explored in the present article.

Figure 1a shows the two types of arrays that were fabricated for this study. These arrays have an SPP resonance mode in the 470–550 nm range, squarely within the visible region of the electromagnetic spectrum[21,22]. The device surface is similar to a conventional microscope slide and the nanofabricated arrays were encapsulated and protected from the environment by an ultra-thin capping layer. For the sake of brevity, we hereafter refer to these 'nanofabricated microscope slides' simply as 'nanoslides'. All tissue samples were prepared using standard microtomy (see Methods).

Figure 1b, top, shows an image of a 70-nm-thick slice of polymer resin next to a bright-field image of the same sample. In this case, about half of the slide did not contain the nanoaperture array, allowing a side-by-side comparison to be made. Owing to the extraordinary optical contrast provided by the buried nanoapertures, the resin shows up clearly whereas the bright-field image only displays a slight intensity variation. To further investigate this effect, we fabricated a nested chevron structure (Fig. 2a and Extended Data Fig. 2a) composed of optically transparent Pt/C stripes of 3, 8, 13 and 19 nm thickness. Figure 2b shows images using the nanoslide (circular apertures) compared to an identical structure on a glass microscope slide; both images were collected in transmission bright-field mode. Atomic force microscopy (AFM) measurements (Extended Data Fig. 2c) confirmed the thickness of the chevrons (features I–IV, Fig. 2b). Figure 2c shows the spectra collected for each stripe individually, within the 400–800 nm range in transmission mode, which can also be reproduced in our finite element modelling (FEM) simulations (Extended Data Fig. 1). Owing to the extraordinary optical contrast effect, variations in Pt/C thickness down to 3 nm are easily detectable. On a conventional glass microscope slide, the intensity difference due to the 13-nm-thick chevron can no longer be detected above background. Figure 2d compares the normalized transmitted intensity collected from the chevron sample when on top of the nanoslide and when on top of a glass microscope slide. The images on the nanoslide show both striking colour variation and increased attenuation using the same source. We note the possibility of identifying different materials by the colour transmitted, as this is characteristic of the dielectric constant of the material. For example, equation (1) (see Methods section 'SPP theory') may be used to calculate $\lambda_{SPP,s}$ (the SPP resonant mode of the sample), thereby providing a measurement of the dielectric constant for the Pt/C chevrons. In this way, we obtain a value for the dielectric constant of 6.9 ± 0.7, consistent with the value for a Pt-containing diamond-like-carbon matrix which, based on the Maxwell–Garnett approximation, is 6.66 (ref. [23]). The increased attenuation is due to plasmon interactions, which enhance the cross-section for light absorption. This effect has previously been observed at near-infrared wavelengths[24,25]. In this example, the intensity contrast alone (see equation (8) in Methods) as a result of the nanoslide increases by a factor of 3.5 compared with the glass microscope slide.

The variation in contrast as a function of the distance from the surface of the nanoslide was investigated. A sample consisting of steps of hydrogen silsesquioxane (HSQ) of known thickness was fabricated and covered by thin Pt/C stripes on top of a nanoslide (Fig. 2e and Extended Data Fig. 2b). The device contained a rectangular array of cross-shaped nanoapertures with the incident light polarized along the 0° direction. AFM measurements (Extended Data Fig. 2d) showed the height of each HSQ step is 35 ± 1 nm and that the thickness of the two Pt/C stripes is 3 ± 1 nm and 11 ± 1 nm, respectively. We chose these thickness values to be close to the thinnest stripe detected using the nanoslide (3 nm) and the thinnest stripe detected using conventional bright-field imaging (11 nm) in Fig. 2a–c. The corresponding background spectrum for all bright-field microscopy presented in this paper is shown in Supplementary Fig. 1.

Both the intensity line scans (Fig. 2f) and the wavelength shifts (Fig. 2g) show the greatest changes closest to the nanoslide surface and the least change when the sample is furthest away, showing that with each step towards the surface the specimen both absorbs more light and the spectrum of the transmitted visible light shifts. The intensity contrast (see equation (8) in Methods) increases from 0.4 to 0.9 while the wavelength shift $\Delta\lambda$ (see equation (1)), which determines the position of the peak transmission wavelength, increases from 10 ± 1 nm to 45 ± 1 nm as the distance of the sample from the surface decreases from 175 ± 1 nm to $10 \text{ nm} \pm 1$ nm. From equation (1) we are able to calculate theoretical curves for $\Delta\lambda$ that provide a good fit to the experimental data in Fig. 2g. The data show that the evanescent electromagnetic field produced by the SPPs had a decay length l_d of about 225 nm, close to the theoretical calculated value of 240 nm, implying that samples which have a thickness larger than this will shift the transmitted wavelength by essentially the maximum possible amount (see Supplementary Fig. 2). We note that for samples of thickness $>l_d$, any height variations at the sample surface are unlikely to lead to a detectable colour change.

Histoplasmonics using a mouse model

To test the application of histoplasmonics to cancer detection in a clearly defined disease state, we used the MMTV-PyMT model of spontaneous breast tumorigenesis, where mammary tumours develop

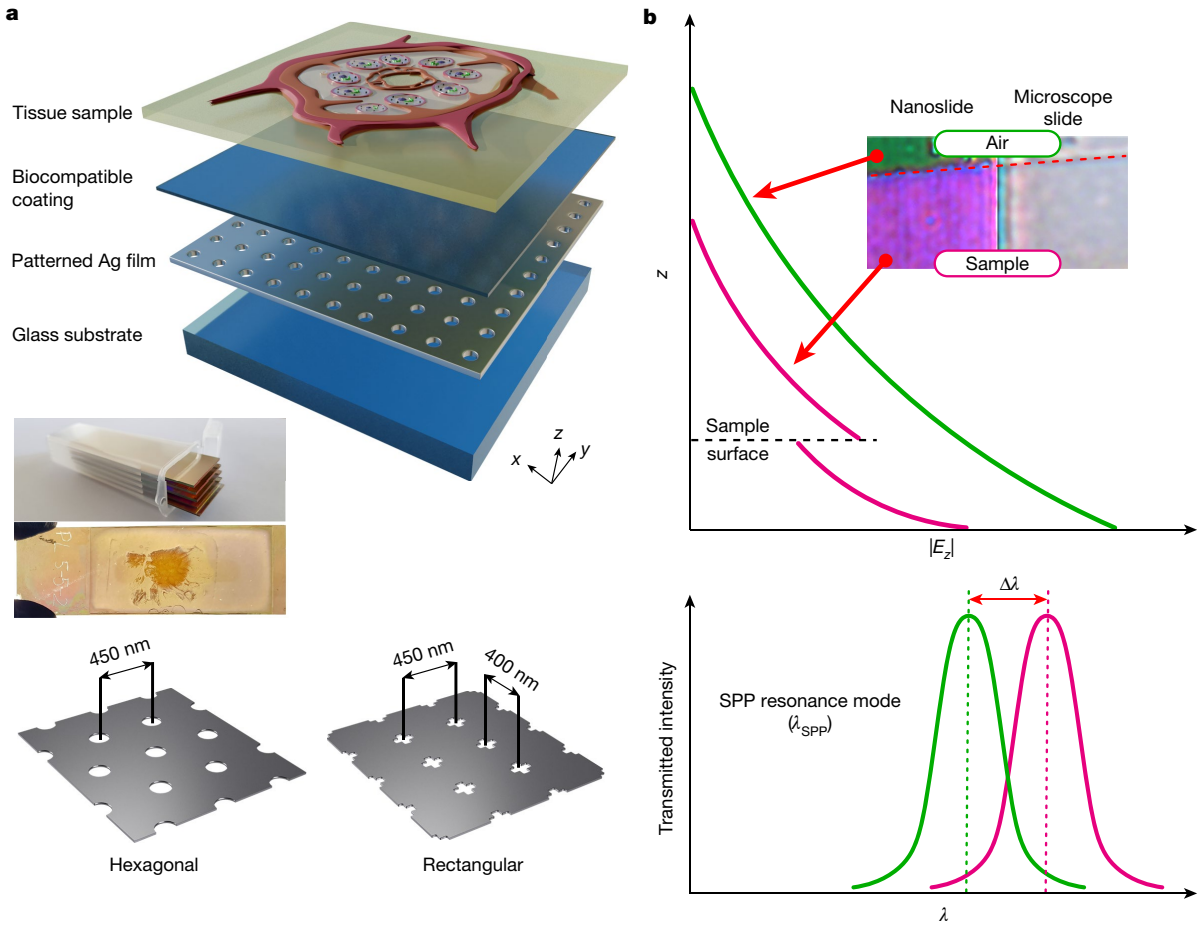

Fig. 1 | Conceptual design and fundamental principles. a, Top, conceptual layered design of the nanoslide; bottom, the two Ag array patterns (thickness = 150 nm), namely, hexagonal and rectangular. Inset, two photographs showing the final nanoslides (75 mm × 25 mm) used for these measurements. The circular nanoaperture diameter is 160 nm. For the cross-shaped nanoapertures, the maximum width of the aperture is 160 nm with each bar being 40 nm across. **b**, Top, schematic of the exponential dependence of the magnitude of the *z* component of the electric field, $|E_z|$, as a function of distance from the nanoslide surface. The decay behaviour both with (magenta curve) and without (green curve) a sample in place is shown. Note there is a discontinuity at the sample surface due to the abrupt change in dielectric constant. An image of a 70-nm slice of resin is shown extending across both a conventional microscope slide and the nanoslide. The resin covers the bottom two-thirds of the image labelled 'sample' while the top of the image is bare and labelled 'air'; the red dashed line denotes the boundary between the two. Bottom, the wavelength of the SPP resonance mode is extremely sensitive to the local dielectric constant, illustrated schematically by the two curves.

through the discrete stages of hyperplasia, mammary intraepithelial neoplasia (MIN) and invasive disease within 50 days of age. This model allowed us to determine if our approach could distinguish between benign and neoplastic states in breast epithelial cells. While the PyMT model is driven by a viral oncoprotein and progresses through a linear series of hyperplasia and invasion, and hence lacks some of the morphological complexities of human pathology, it is a widely employed model for analysing the cellular changes that occur in early breast cancer. A key advantage of this model system is that the proliferative marker Ki67 serves as a robust biomarker for distinguishing normal epithelium from hyperplasia and neoplasia[26], allowing a clear benchmark for our initial comparisons using histoplasmonics.

In total, 24 mammary tissues derived from six MMTV-PYMT$^+$ mice were used for this study (see Extended Data Fig. 3 and Methods). The differences in the spectral output between benign and neoplastic breast tissue giving rise to colour contrast are illustrated in Fig. 3a. On the basis of the 24 MMTV-PyMT$^+$ mammary tissue sections studied, the spectral output of cancer cells appears to have good differentiation compared to other types of non-cancerous epithelial cells, providing a promising mechanism for aiding digital pathology[27–29]. In particular, using the hue, saturation, lightness (HSL) image pixel colour space values, it is possible to digitally analyse the images in a similar fashion to previous immunohistochemistry (IHC) staining-based studies[30]. To further validate the pathology results against published standards, we used an established scoring matrix[26] (see Methods) for discriminating 'normal', hyperplasia, MIN and invasive lesions in the MMTV-PyMT model. As revealed in results presented in Fig. 3d, both approaches (nanoslide and Ki67) identify a similar (albeit consistently higher in the case of nanoslide) percentage of neoplastic cells in a randomized preclinical study (see Methods). We ascribe the sensitivity of histoplasmonics to the cancer cells as being due to their differing cellular density leading them to develop a contrasting dielectric constant[27–29] along with the change in their morphology.

Figure 3b shows the colorimetric analysis of 'healthy' and 'invasive cancer' tissue (classification is based on expression of Ki67, see Supplementary Table 1) using histoplasmonics based on the measured hue (*H*, in degrees) and luminosity (*L*, in %) of the images. Note that the 'healthy' (Ki67 positivity between 0% and 28%) tissue sections are taken from MMTV-PyMT mice, 90% of which will eventually develop pre-invasive and invasive neoplasms. This is distinct from 'normal' tissue sections, which are derived from non-tumour-bearing mice and hence are not expected to later develop cancer. Therefore, while no overlap is observed between normal (PyMT$^-$ wild-type mice) and neoplastic (MMTV-PyMT$^+$) tissue, a small amount of overlap is anticipated

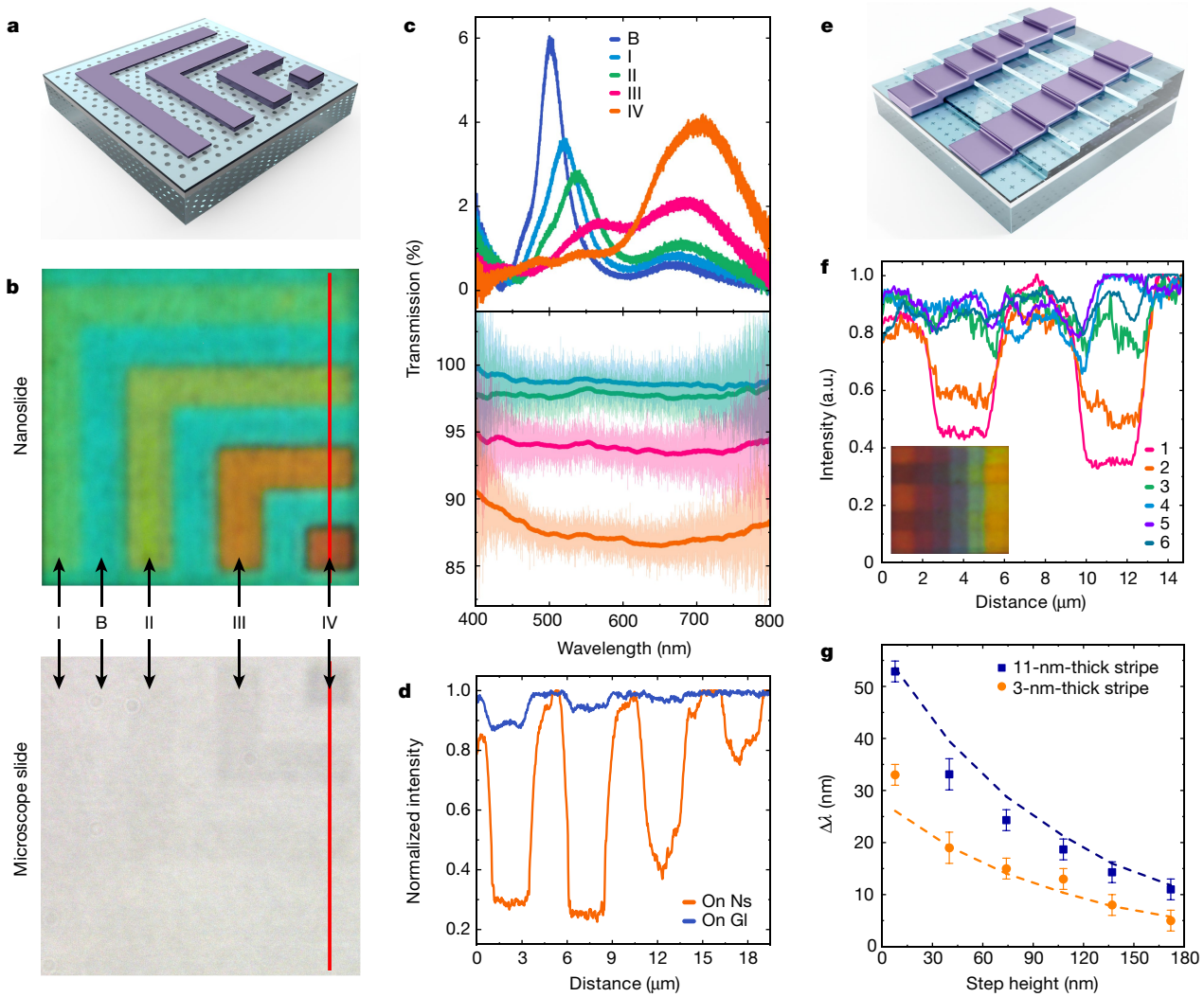

Fig. 2 | Testing device sensitivity using nanofabricated samples. **a**, Conceptual design of the 'chevron sample'. Four Pt/C chevrons of different thicknesses were deposited on the nanoslide, the thinnest sample stripe being 3 ± 1 nm. **b**, Optical bright-field images. An identical sample covers both nanoslide and a conventional glass microscope slide. Indicated are chevrons I–IV, and background B. **c**, Transmission spectra collected from each of the four chevrons and the background, collected from the nanoslide (top) and the glass microscope slide (bottom). The solid lines are moving averages (200 points) to guide the eye. **d**, An intensity line scan across the four chevrons (Ns, nanoslide, Gl, glass microscope slide); the position of the line scan is shown as a red line in the upper and lower panels of **b**. **e**, Conceptual design of the 'staircase sample'. Two Pt/C stripes of different thicknesses were deposited on the nanoslide on top of an HSQ 'staircase' made up of six steps. **f**, Intensity line scans across the Pt/C stripes for all six steps (1 is the closest to the surface and 6 is the furthest away). Inset, the corresponding bright-field optical image, moving from the thinnest to the thickest step, left to right. **g**, $\Delta\lambda$ as a function of step height for the two stripes (of thickness 3 ± 1 nm and 11 ± 1 nm). The error bars are the s.d. The dashed lines shows the fits generated from SPP theory (see equation (1) and Methods). The results show that, for a Pt/C stripe of a given thickness, a thicker HSQ step produces a smaller $\Delta\lambda$, as expected.

between the 'healthy' and invasive cancer regions. This highlights the fact that there is a continuum in morphology between the different stages and the fact that these are not truly 'normal' tissues. The origins of the small overlap in terms of the hue and luminosity between the 'healthy' tissue and the cancerous will form the basis of future investigations and may be informative for other settings, in other tumour types. The difference between normal and neoplastic mammary epithelial cells supports discrimination between normal and neoplastic tissue. There also appears to be a difference in the colorimetric properties of healthy (pre-cancerous) epithelium and the mammary glands of non-tumour-bearing 'normal' mice, indicating a potential application to the early diagnosis of pre-malignancy.

To test the concordance of Ki67 and histoplasmonics, we compared the percentage (by area) of tissue identified by pathologists as containing neoplastic cells according to the image pixel HSL colour space values (Fig. 3c). The positive correlation between Ki67 and histoplasmonics supports the pathology scoring (Fig. 3d) and concurs with the Sørensen–Dice coefficients (Fig. 3e). Together, the data support our hypothesis that our approach can aid in the discrimination of neoplastic cells in a model system that, unlike human pathology, utilizes Ki67 as a benchmark.

Histoplasmonics using a DCIS patient cohort

Use of mouse models supported nanoslide as a potential platform for distinguishing cancer cells from normal cells in mice. However, such models do not recapitulate the nonlinear nature of early breast cancer pathology or the intra- and inter-patient variability in disease morphology and pathogenesis. Additionally, markers such as Ki67 are not useful for diagnosis in this setting. To determine if histoplasmonics could help to distinguish neoplastic breast epithelium from benign or normal tissues, retrospective breast cancer samples taken at the

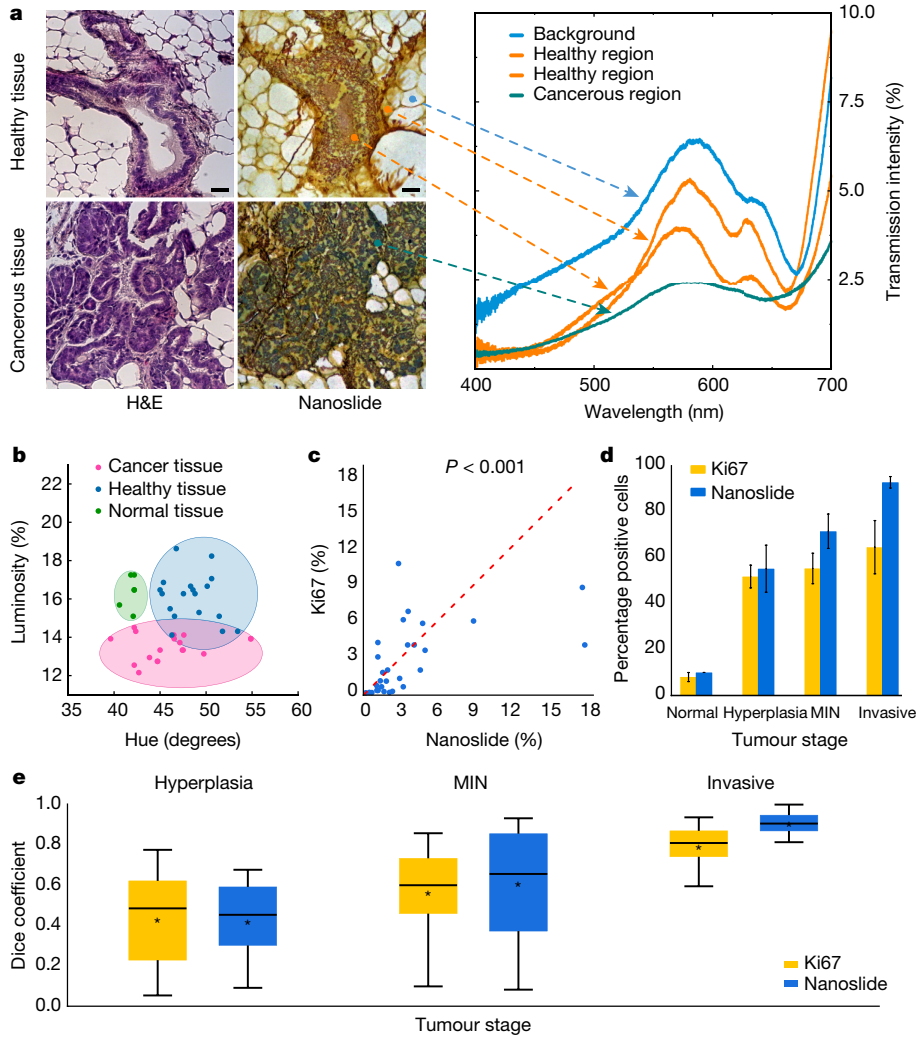

Fig. 3 | Quantification of spectral output, comparison to Ki67, pathology scoring and statistics. a, Characteristics of healthy and cancerous tissue. Left, micrographs of H&E stained tissue, and nanoslide images. Right, spectral characteristics taken from the areas shown by dots in **a**. Scale bar, 15 µm. **b**, Regions evaluated by histopathology plotted as a function of luminosity versus hue. **c**, Comparison of percentage of cancerous cells identified on the basis of HSL colour space values using Ki67 (vertical axis) and nanoslide (horizontal axis) (see Methods). The Pearson correlation coefficient, *r*, and corresponding *P* value for the Ki67 and nanoslide results confirm a positive correlation: $r(28) = 0.62$, $P < 0.001$. All data were analysed using GraphPad Prism software (v.9.0.2). **d**, Pathology scoring of Ki67 and nanoslide for data collected from 24 tissue sections (derived from $N = 6$ mice in total), the percentage of cells identified as cancerous is indicative of the tumour stage (see Methods and Supplementary Table 1). Data shown as mean ± s.e.m. **e**, Dice coefficients (equation (10)) for nanoslide and Ki67 for three different classes of neoplastic region. The boxes indicate the lower quartile, the median and the upper quartile. The whiskers indicate respectively the smallest and largest observation. The mean is indicated by the black markers. These were calculated for both nanoslide and Ki67 based on the analysis of 64 different tissue regions.

time of diagnosis, incorporating normal and benign UDH tissues, were interrogated. We used a retrospective cohort ($N = 24$ patients in total) of normal ($N = 6$), UDH ($N = 6$), DCIS ($N = 6$) and invasive ($N = 6$) tissues derived from patients with a previously confirmed pathology diagnosis based on the 'gold standard' H&E-based morphological assessment. The workflow for the study design is shown in Fig. 4a, while the harvesting of serial sections for direct comparison of nanoslide, H&E and Ki67 is illustrated in Extended Data Fig. 8.

A particularly important aspect of this study was to determine if histoplasmonics could aid in differentiating normal epithelial cells from DCIS, an early stage of breast cancer that now represents 20–25% of mammogram-detected breast cancer cases[31]. DCIS comprises lesions that are heterogeneous with highly variable morphology[32]; whereas at the extremes of normal and invasive, breast cancer is generally easy to discern, low-grade DCIS can be subtle. Hence, while a trained pathologist examining H&E-stained slides constitutes the 'gold standard' for diagnosis, locating and identifying suspect lesions is challenging, and consequently early-stage breast cancer tissues may suffer from misdiagnosis based on H&E alone[33]. Because it fits into existing pathology workflows, nanoslide could be used in a clinical setting as an adjunct to H&E staining, improving cancer specificity and potentially reducing rates of misdiagnosis while also reducing the manual labour and tissue preparation time required for IHC[34]. In particular, it could potentially replace or support markers such as cytokeratin 5 and 6 (CK 5/6) and the oestrogen receptor (ER) that may be currently used to assist distinguishing UDH from atypical ductal hyperplasia (ADH) and low-grade DCIS.

Serial section comparison of H&E and nanoslide revealed differences between the nanoslide 'staining' of normal and malignant epithelial cells (Fig. 4b). Upon analysis of UDH and DCIS, an increase in nanoslide staining was observed in DCIS lesions, coinciding with changes to CK 5/6 and ER expression (Fig. 4c, d). The percentage of nanoslide-positive epithelial cells across the cohort was pathology-scored and is presented in Fig. 4e. Importantly, there was a difference in staining frequency between non-cancer and other states, supporting the results from

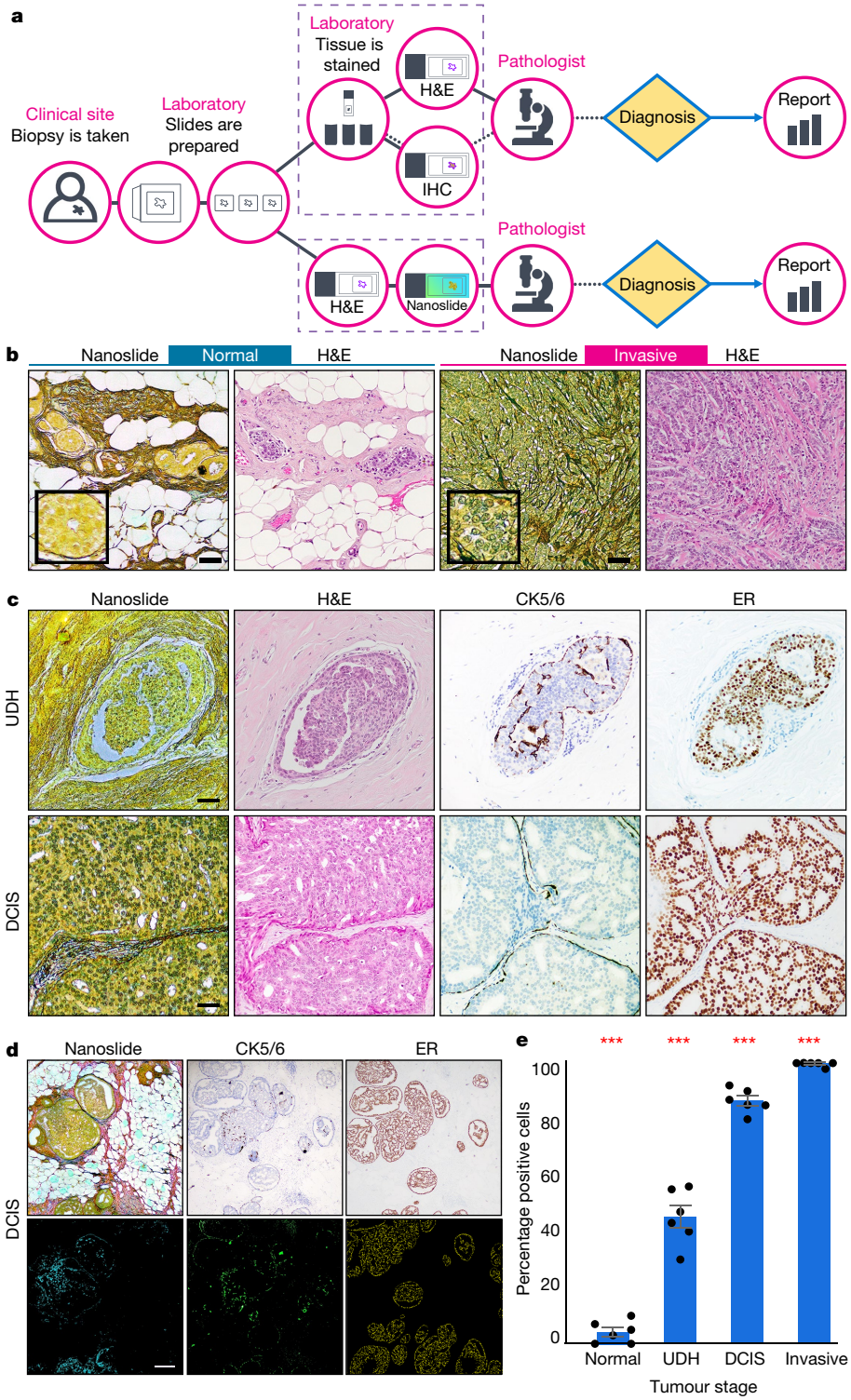

Fig. 4 | Nanoslide histology images and pathology assessment of retrospective DCIS human cohort. a, Pathology workflow for DCIS retrospective cohort study. **b**, Comparison of high-resolution (scale bar, 20 µm) nanoslide and H&E stained images for healthy, non-cancer and invasive breast cancer tissues. The boxes represent higher-magnification regions of the tissue (60 µm × 60 µm). **c**, Comparison of high-resolution (scale bar, 20 µm) images of UDH (top) and DCIS (bottom) using four different techniques: nanoslide, H&E staining, IHC-based detection of CK 5/6 and ER. **d**, Comparison of lower magnification (scale bar, 200 µm) images of the nanoslide, CK 5/6 and ER techniques. IHC detection of CK5/6 and ER is indicated by brown (DAB) staining; tissues are counterstained with haematoxylin (blue) **e**, Summary of scoring ($N = 24$ patients in total) for healthy (control) tissue ($N = 6$), UDH ($N = 6$), DCIS ($N = 6$) and invasive cancer state ($N = 6$). A statistically significant difference between groups was confirmed by a one-way analysis of variance (ANOVA) test ($F(2,27) = 235.679$). A Games–Howell post hoc test also revealed that the pairwise comparisons between the three groups (UDH, DCIS and invasive cancer state) are all significant (***$P < 0.001$). The error bars represent s.e.m.

the mouse study that histoplasmonics can help differentiate between normal and cancerous cells (both DCIS and invasive). Additionally, our work supports future studies into the utility of this technique as an adjunct diagnostic for diagnosing UDH versus DCIS, since a difference in the staining frequency in these pathologies was also detected.

The combined data support histoplasmonics as a potential label-free alternative for differentiating breast cancer cells from normal epithelial cells or a benign state, which could also readily be extended to other cancer types. Treating and labelling samples with the appropriate IHC can take anywhere from several hours up to several days[34], substantially delaying diagnosis and generally preventing the use of IHC biomarker staining in intraoperative pathology. The introduction of nanoslide could not only eliminate the need for IHC staining, but could also reduce the dependence on IHC-based cancer-specific biomarkers. This is particularly important given the lack of cancer-specific biomarkers available to identify heterogeneous cancer types or subtypes. Hence, a cancer marker, based on nanotechnology rather than IHC staining, which could help to distinguish benign or reactive conditions and malignant lesions, would have a very high clinical utility. We note that the rapid visualization of cells by nanoslide is also effective in very fine tissue sections—for example, those typically used for transmission electron microscopy (see Methods and Extended Data Fig. 9).

In conventional optical microscopy the sample rarely exhibits strong colours except when dyes are added, in which case the sample typically presents as a uniform colour. In histoplasmonics, the sample's dielectric constant plays an active role in determining the observed colour, generating striking high-contrast, full-colour images. This approach to histology could provide instant feedback and entirely new information, leading to the development of novel diagnostics at the point-of-care. Furthermore, we have found that polarization control allows us to actively select specific features or cells within the sample. In addition to viewing static samples, it may also be possible to track dynamic cellular processes, without the need for any staining or labelling. In spite of the heterogeneity typically present in the samples studied here, the current implementation of histoplasmonics appears to enable a surprising degree of cancer specificity comparable to, or even surpassing, the IHC we benchmarked against. In the context of diagnosis of UDH versus DCIS, future studies are planned using larger cohorts to confirm the diagnostic settings where histoplasmonics will have clinical utility. However, we emphasize that although the nanoslides employed here have been optimized for visible light imaging of tissues, there is nothing specific about the design that would preclude their application to any other type of optically transparent sample, including materials science or even engineering specimens.

Online content

Any methods, additional references, Nature Research reporting summaries, source data, extended data, supplementary information, acknowledgements, peer review information; details of author contributions and competing interests; and statements of data and code availability are available at https://doi.org/10.1038/s41586-021-03835-2.

1. Judd, D. B. & Wyszecki, G. *Color in Business, Science, and Industry* (Wiley & Sons, 1975).
2. Alberts, B. *Molecular Biology of the Cell* (Garland Science, Taylor & Francis, 2008).
3. Fu, Y., Tippets, C. A., Donev, E. U. & Lopez, R. Structural colors: from natural to artificial systems. *Wiley Interdiscipl. Rev. Nanomed. Nanobiotechnol.* **8**, 758–775 (2016).
4. Lochbihler, H. Colored images generated by metallic sub-wavelength gratings. *Opt. Express* **17**, 12189–12196 (2009).
5. Lee, H.-S., Yoon, Y.-T., Lee, S.-S., Kim, S.-H. & Lee, K.-D. Color filter based on a subwavelength patterned metal grating. *Opt. Express* **15**, 15457–15463 (2007).
6. Inoue, D. et al. Polarization independent visible color filter comprising an aluminum film with surface-plasmon enhanced transmission through a subwavelength array of holes. *Appl. Phys. Lett.* **98**, 093113 (2011).
7. Duempelmann, L., Casari, D., Luu-Dinh, A., Gallinet, B. & Novotny, L. Color rendering plasmonic aluminum substrates with angular symmetry breaking. *ACS Nano* **9**, 12383–12391 (2015).
8. Raj Shrestha, V., Lee, S.-S., Kim, E.-S. & Choi, D.-Y. Polarization-tuned dynamic color filters incorporating a dielectric-loaded aluminum nanowire array. *Sci. Rep.* **5**, 12450 (2015).
9. Liddle, J. A. & Gallatin, G. M. Nanomanufacturing: a perspective. *ACS Nano* **10**, 2995–3014 (2016).
10. Vala, M. & Homola, J. Flexible method based on four-beam interference lithography for fabrication of large areas of perfectly periodic plasmonic arrays. *Opt. Express* **22**, 18778–18789 (2014).
11. Wang, L. et al. Large area plasmonic color palettes with expanded gamut using colloidal self-assembly. *ACS Photon.* **3**, 627–633 (2016).
12. Franklin, D. et al. Polarization-independent actively tunable colour generation on imprinted plasmonic surfaces. *Nat. Commun.* **6**, 7337 (2015).
13. Solak, H. H., Dais, C. & Clube, F. Displacement Talbot lithography: a new method for high-resolution patterning of large areas. *Opt. Express* **19**, 10686–10691 (2011).
14. Choudhury, K. R., Yagle, K. J., Swanson, P. E., Krohn, K. A. & Rajendran, J. G. A robust automated measure of average antibody staining in immunohistochemistry images. *J. Histochem. Cytochem.* **58**, 95–107 (2010).
15. Wong, T. T. W. et al. Fast label-free multilayered histology-like imaging of human breast cancer by photoacoustic microscopy. *Sci. Adv.* **3**, e1602168 (2017).
16. Fereidouni, F. et al. Microscopy with ultraviolet surface excitation for rapid slide-free histology. *Nat. Biomed. Eng.* **1**, 957–966 (2017).
17. Neilson, K. A. et al. Less label, more free: approaches in label-free quantitative mass spectrometry. *Proteomics* **11**, 535–553 (2011).
18. Lu, F.-K. et al. Label-free DNA imaging in vivo with stimulated Raman scattering microscopy. *Proc. Natl Acad. Sci. USA* **112**, 11624–11629 (2015).
19. Ji, M. et al. Rapid, label-free detection of brain tumors with stimulated Raman scattering microscopy. *Science Transl. Med.* **5**, 201ra119 (2013).
20. Lee, M. et al. Label-free optical quantification of structural alterations in Alzheimer's disease. *Sci. Rep.* **6**, 31034 (2016).
21. Langley, D. P., Balaur, E., Hwang, Y., Sadatnajafi, C. & Abbey, B. Optical chemical barcoding based on polarization controlled plasmonic nanopixels. *Adv. Funct. Mater.* **28**, 1704842 (2018).
22. Langley, D., Balaur, E., Sadatnajafi, C. & Abbey, B. Dual pitch plasmonic devices for polarization enhanced colour based sensing. *Proc. SPIE* **10013**, 1001338 (2016).
23. Huth, M. et al. Focused electron beam induced deposition: a perspective. *Beilstein J. Nanotechnol.* **3**, 597–619 (2012).
24. Ding, X. et al. Surface plasmon resonance enhanced light absorption and photothermal therapy in the second near-infrared window. *J. Am. Chem. Soc.* **136**, 15684–15693 (2014).
25. Kawata, S., Ichimura, T., Taguchi, A. & Kumamoto, Y. Nano-Raman scattering microscopy: resolution and enhancement. *Chem. Rev.* **117**, 4983–5001 (2017).
26. Duivenvoorden, H. M., Spurling, A., O'Toole, S. A. & Parker, B. S. Discriminating the earliest stages of mammary carcinoma using myoepithelial and proliferative markers. *PLoS ONE* **13**, e0201370 (2018).
27. Wang, Z., Tangella, K., Balla, A. & Popescu, G. Tissue refractive index as marker of disease. *J. Biomed. Opt.* **16**, 116017 (2011).
28. Shan, M., Kandel, M. E. & Popescu, G. Refractive index variance of cells and tissues measured by quantitative phase imaging. *Opt. Express* **25**, 1573–1581 (2017).
29. Giannios, P. et al. Visible to near-infrared refractive properties of freshly-excised human-liver tissues: marking hepatic malignancies. *Sci. Rep.* **6**, 27910 (2016).
30. Shi, P. et al. Automated Ki-67 quantification of immunohistochemical staining image of human nasopharyngeal carcinoma xenografts. *Sci. Rep.* **6**, 32127 (2016).
31. van Seijen, M. et al. Ductal carcinoma in situ: to treat or not to treat, that is the question. *Br. J. Cancer* **121**, 285–292 (2019).
32. Elmore, J. G. et al. Diagnostic concordance among pathologists interpreting breast biopsy specimens. *J. Am. Med. Assoc.* **313**, 1122–1132 (2015).
33. Simpson, P. T., Reis-Filho, J. S., Gale, T. & Lakhani, S. R. Molecular evolution of breast cancer. *J. Pathol.* **205**, 248–254 (2005).
34. Ramkumar, C., Prakash, C., Madhav, L., Kumar, A. & Basavaraj, C. Assessment of Ki67 as a prognostic marker in hormone receptor positive breast cancer: a retrospective study on an Indian cohort. *J. Mol. Biomark. Diagn.* (2017).

Methods

Devices and characterization

FEM modelling in the COMSOL Multiphysics package (version 5.6) was used to optimize the device design and confirm our fundamental understanding of the chromatic contrast enhancement effect. The periodic arrays of nanoapertures were fabricated using the focused ion beam (FIB) lithography technique (Helios NanoLab 600 Dual Beam FIB-SEM, FEI) for small areas, or displacement Talbot lithography for large areas[35]. The devices were fabricated in 150-nm-thick Ag films, using circular nanoapertures (450-nm period) on a hexagonal pattern and cross-shaped nanoapertures on a rectangular pattern[36,37]. The cross-shaped nanoapertures had a 450-nm period in one direction (defined here as the 0° direction) and a 400-nm period in the orthogonal direction (defined as the 90° direction). To protect the surface, a very thin layer (10 ± 1 nm) of either SiO_2 or hydrogen silsesquioxane (HSQ), a glass-like material, was deposited as the final step after fabrication[38]. The HSQ protective layer was spun after the array fabrication. HSQ was converted into amorphous silicon oxide via exposure to electrons[38].

The Pt/C deposition was performed by means of the electron-beam induced deposition method (EBID) using trimethyl(methylcyclopentadienyl)platinum as the precursor gas[39]. The EBID method enables precise control over the thickness of the deposited structures (in the 1 nm range) with minimum residue left. For the staircase-like sample, after HSQ treatment, we used the FIB to mill a structure comprising six steps of different thickness. Subsequently, two Pt/C stripes were deposited on top. Large-area samples were covered with 10-nm SiO_2 deposited by EBID. Bright-field and differential interference contrast data were collected using a Nikon Ti-U microscope system; spectral data were collected using an IsoPlane SCT 320 (Princeton Instruments) at 1,200 lines per mm. The spectral data were normalized with respect to the bare substrate. A Bruker Dimension Icon AFM was used to collect the topographical data and line scans.

SPP theory

The spectral output of the nanoslides is determined by the SPP resonant modes, $\lambda^{\theta}_{\mathrm{SPP},d}$, where θ denotes the incident polarization angle (the symbol is removed for unpolarized light) and the subscript indicates whether the dielectric constant is for the sample (d = s) or for air (d = a). The SPP modes are characterized by peaks in the transmission spectra (Fig. 1b); the corresponding wavelength shift ($\Delta\lambda$) relative to air when a sample of thickness t is placed on top of the nanoapertures is given by[40]

$$\Delta\lambda \approx \left(\lambda^{\theta}_{\mathrm{SPP,s}} - \lambda^{\theta}_{\mathrm{SPP,a}}\right)\left(1 - \exp\left(-\frac{2t}{l_{\mathrm{d}}}\right)\right), \tag{1}$$

where $l_{\mathrm{d}} \approx \lambda/2\sqrt{\varepsilon_{\mathrm{d}}}$ is the characteristic decay length of the SPP electromagnetic field, which is itself a function of ε_{d}, the dielectric constant of the sample. The periodicity of the nanoaperture array dictates the wavelength range within which the plasmon resonances occur. In the present case the periodicity was selected to ensure the primary resonance peak was within the middle of the visible spectrum. The nanoaperture diameter and shape principally determine the amount of light transmitted and the width of the resonance peaks. Here, we opted for the smallest aperture sizes possible while maintaining a practical amount of light transmission (for example, to maintain data collection times of less than 1 s per image). One of the current limitations of the theory of SPPs is that it does not account for the aperture shape. However, FEM of the transmission of light through our array indicates that the shape of the individual nanoapertures does not appreciably alter the position of the SPP modes (see Extended Data Fig. 1).

Consider a hexagonal nanoaperture array (450-nm period) fabricated in an Ag film; the $\lambda_{\mathrm{SPP,a}}$ for this array is 500 nm. If the sample is composed of polycarbonate ($C_{16}H_{18}O_5$), then $\lambda_{\mathrm{SPP,s}}$ = 750 nm and l_{d} = 240 nm; for a 10-nm-thick film, equation (1) predicts that the transmitted SPP resonance mode in air will undergo a red-shift of around 20 nm resulting in a visually distinct colour change. As the film thickness increases, the transmission SPP resonance peak is increasingly red-shifted until it equals $\lambda_{\mathrm{SPP,s}}$ (that is, when $t = l_{\mathrm{d}}$) after which no more colour change occurs.

The generation of SPPs in the nanoslides can be understood in terms of an electromagnetic (EM) wave propagating through an array of metallic nanoapertures with a dielectric material in contact with the array (Fig. 1a). Here we define the 'half-space' of the device as a portion of the 3D space lying on one side of a 2D interface, which lies in the z = 0 plane. The localized EM field of SPPs at the metal–dielectric interface decays exponentially into both half-spaces with increasing distance from the interface. The dispersion relation in the half space of both the metal (n = m) and dielectric (n = d) for the electric field at time τ is

$$E_{m,n} = \begin{pmatrix} E_{x,n} \\ 0 \\ E_{z,n} \end{pmatrix} \mathrm{e}^{i|k_x|x + i|k_{z,n}||z| - i\omega\tau}, \tag{2}$$

where E denotes the amplitude of the field components whose direction is indicated by m (either x or z) and $\mathbf{k}$ is the wavevector in the plane of the nanoaperture array (the wave oscillates in the x direction and decays exponentially in the z direction). $\mathbf{k}_x$ is identical for both metal and dielectric, but $\mathbf{k}_{z,\mathrm{m}} \neq \mathbf{k}_{z,\mathrm{d}}$; ω is the angular frequency. By enforcing the condition that the wave described by equation (2) must satisfy Maxwell's equations, an approximate solution for $\mathbf{k}_x$ is obtained, which is the dispersion relation for a wave propagating at the metal–dielectric interface[41]:

$$|k_x| \approx \frac{\omega}{c}\sqrt{\frac{\varepsilon_{\mathrm{m}}\varepsilon_{\mathrm{d}}}{\varepsilon_{\mathrm{m}} + \varepsilon_{\mathrm{d}}}} \tag{3}$$

For a lattice array containing two different periods, SPPs are excited when their momentum matches the momentum of the incoming photons and the grating, that is, when $\mathbf{k}_{\mathrm{SPP}} = \mathbf{k}_x \pm i\hat{\mathbf{G}}_x \pm j\hat{\mathbf{G}}_y$ where $\mathbf{k}_{\mathrm{SPP}}$ is the corresponding plasmon wavevector, and where i and j are integers, which define the orders for grating momentum unit wavevectors for a rectangular array $\hat{\mathbf{G}}_x$ and $\hat{\mathbf{G}}_y$ respectively. Therefore, if the wavelength of the incident light is varied, different SPP modes are excited[42]. In this paper we typically refer to the primary SPP mode (i = 1; j = 0), whose corresponding wavelength at normal incidence lies within the visible range and is given by[40]

$$\lambda^{\theta}_{\mathrm{SPP},d} \approx \frac{P_{\theta}}{\sqrt{i^2 + j^2}}\sqrt{\frac{\varepsilon_{\mathrm{m}}\varepsilon_{\mathrm{d}}}{\varepsilon_{\mathrm{m}} + \varepsilon_{\mathrm{d}}}} \tag{4}$$

for a rectangular array, which varies with the incident polarization[43], and by

$$\lambda_{\mathrm{SPP},d} \approx \frac{P\sqrt{3}}{2\sqrt{i^2 + j^2 + ij}}\sqrt{\frac{\varepsilon_{\mathrm{m}}\varepsilon_{\mathrm{d}}}{\varepsilon_{\mathrm{m}} + \varepsilon_{\mathrm{d}}}} \tag{5}$$

for a hexagonal array, which is independent of the incident polarization. Here P defines the array periodicity, and ε_{m} and ε_{d} (discussed in the main text) are the dielectric constants of the metal and dielectric respectively. Note that $\lambda^{\theta}_{\mathrm{SPP},d}$ corresponds to a peak maximum in the transmission spectrum for the rectangular array at θ = 0° or θ = 90°, when one of the primary modes for the two periods of the array is excited. In addition, the calculation of $\lambda^{\theta}_{\mathrm{SPP},d}$ assumes an infinitely thick dielectric layer. At intermediate polarizations, the resulting transmission spectrum is a linear combination of the spectra at θ = 0° and θ = 90° (equations (6) and (7)):

$$|\mathbf{E}_z(\theta)|^2 = |\mathbf{E}_z(0°)|^2\cos^2\theta + |\mathbf{E}_z(90°)|^2\sin^2\theta \quad (6)$$

$$\mathbf{H}_z(\theta) = \mathbf{H}_z(0°)\cos\theta + \mathbf{H}_z(90°)\sin\theta \quad (7)$$

where $\mathbf{E}_z$ and $\mathbf{H}_z$ are the z components of the electric and magnetic fields respectively. In this case other resonances may dominate such that $\lambda^{\theta}_{SPP,d}$ no longer corresponds to a peak maximum. In this paper we only present results from cases where $\theta = 0°$ or $\theta = 90°$. A discussion of the intermediate case, in terms of the resultant spectra, is provided in ref. [22]. Determining the value of $\lambda^{\theta}_{SPP,d}$ for a given array periodicity involves finding the particular wavelength which satisfies equation (3). Since both $\lambda^{\theta}_{SPP,d}$ and ε_m depend on the same variable (λ), this is achieved via either iterative or graphical methods.

Intensity contrast

Image intensity contrast is defined here as the root mean square (RMS) intensity, C_{RMS}, which does not depend explicitly on the frequency content of the image and is defined as

$$C_{RMS} = \sqrt{\frac{1}{ab}\sum_{x=0}^{a-1}\sum_{y=0}^{b-1} I(x,y) - \bar{I}}, \quad (8)$$

where $I(x,y)$ is the intensity value at coordinate (x,y) in an image of size $a \times b$ with an average intensity given by $\bar{I}$.

Mouse models and histoplasmonics

Mouse investigations were performed after approval by the La Trobe University Animal Ethics Committee. The workflow for the study design is shown in Extended Data Fig. 3a while the harvesting of serial sections for direct comparison of nanoslide, H&E and Ki67 is illustrated in Extended Data Fig. 3b. For each 4-µm slice of tissue sectioned and placed on a nanoslide, serial sections were mounted on glass slides for H&E staining and immunohistochemistry (IHC) using a Ki67-specific antibody. This protocol for comparing histological features between adjacent sections of the same tissue[44] allows us to benchmark our approach against Ki67, albeit with a difference of up to 12 µm in terms of tissue depth. Large field-of-view (3.8 mm × 3.8 mm) sections of corresponding slices of H&E, Ki67 and nanoslide images are represented in Extended Data Fig. 4. Further, higher-magnification (0.9 mm × 0.9 mm) images are shown in Supplementary Fig. 3. These sections cover a range of different tissue types (for example, lymph nodes, collagen, muscle tissue, ligament) (Extended Data Fig. 5) and also include regions of pre-invasive and invasive mammary cancer regions, where a contrast in colour is apparent in cancer cells on the stain-free nanoslide. To directly compare nanoslide to benchmark Ki67 staining in the MMTV-PyMT model, the areas of positivity of both nanoslide and Ki67 were identified on the basis of their respective HSL colour space values (see, for example, ref. [45]). Based on the range of HSL values for cancerous tissue using both Ki67 and nanoslide, by exploiting the intrinsic properties of the HSL colour space we were able to threshold the images to predominantly display neoplastic tissue only. The results of carrying out this procedure for nanoslide and Ki67 are shown on the bottom row of Extended Data Fig. 4, illustrating the excellent concordance between Ki67 and nanoslide in this model. Further, we prepared a series of thinner (1 µm thick) sections with near-identical morphology and performed a cell-by-cell comparison of Ki67 and nanoslide positivity (see Extended Data Fig. 7).

Mammary glands were isolated from C57 BL/6 MMTV-PyMT positive female mice at a time when spontaneous mammary tumours develop (50 days old)[46]. Tissues (including those derived from normal C57 BL/6 mice) were fixed in 10% buffered formalin, paraffin embedded and sectioned at 4 µm or 5 µm onto glass slides or nanoslides. For immunohistochemical detection of a proliferative marker, sections (formalin-fixed, paraffin embedded) were dewaxed following standard protocols and stained with anti-Ki67 (1 µg ml^{-1} Abcam, ab15580), following high-temperature and -pressure antigen retrieval in pH 6 sodium citrate buffer, overnight at 4 °C and detected with a biotin-conjugated secondary antibody (Vector Laboratories), followed by DAB staining to reveal antibody binding (brown) and haematoxylin nuclear counter-staining (blue). H&E staining was conducted following standard protocols.

In order to test the performance of nanoslide for very fine (<100 nm thick) tissue sections, typically used for TEM, we used slices of optic nerve tissue embedded in resin (see Extended Data Fig. 9). For the optic nerve samples, transgenic mice were produced by microinjection of a 4.7-kb DNA fragment consisting of 1.3 kb of MBP sequences and 3.4 kb of c-myc genomic DNA including part of intron 1, exons 2 to 3, and 316 bp of 38 untranslated sequences[47]. The 2-50 pedigree carries approximately 10 copies of the construct on chromosome 9 and was isolated on the basis of a shivering phenotype evident in that pedigree alone, out of seven originally generated. The transgenic mice and non-transgenic littermates were perfused through the left ventricle with phosphate-buffered saline at 37 °C for 2 min, followed by 4% paraformaldehyde/2.5% glutaraldehyde in phosphate buffer, pH 7.4 containing 200 IU heparin per100 ml. Tissue was left in situ at 4 °C for 1 h before sections were cut via microtomy. Optic nerves were fixed in 2.5% glutaraldehyde, post fixed in osmium tetroxide and dehydrated in ethanol and acetone before being embedded in epoxy resin. Nanometre-thick sections were cut on a Leica UC7 ultramicrotome.

Pathology assessment

MMTV-PyMT model. To confirm the timing of spontaneous development of mammary gland tumours in the C57 BL/6 MMTV-PyMT model, mammary glands of C57 BL/6 MMTV-PyMT mice at different stages were taken and morphologically evaluated by H&E and Ki67 by a human-breast and murine-mammary-gland pathologist and breast-cancer researcher. Nanoslide samples were randomized and independently scored and then compared post-analysis to the results of Ki67. The benchmark for the pathology assessment was a trained pathologist analysing the H&E stained tissue sections at high resolution and without any time constraints. As this was a control study, the cancer was pathology-confirmed before nanoslide assessment. In addition, use of Ki67 IHC staining allowed confirmation that all neoplastic regions were assessed and aided in individual tumour cell counts. The 'percentage positive cells' across all samples was then determined via comparison of frequency of individual cell positivity for Ki67 or nanoslide (via a colour change—'brown' for Ki67 and 'blue' for nanoslide) compared to total number of cancer cells identified by pathological H&E. Based on pathology diagnosis of cancer stage, results could be classified into four stages: 'normal', 'hyperplasia', 'MIN' and 'invasive'. Data are presented as mean ± s.e.m. (Fig. 3d). The scoring matrix for discriminating normal, MIN and invasive lesions is shown in Supplementary Table 1.

The pathology assessment was carried out by S.O'T. and B.S.P. The assessments were conducted independently, and verified for concordance: $r(4) = 0.98$, $P < 0.003$ (the result is significant at $P < 0.05$) indicating a 'very high' degree of positive correlation between the independent scores.

Retrospective breast cancer patient cohort. Normal breast, UDH, DCIS and invasive breast cancer sections were obtained from routine diagnostic samples taken at RMH and Austin Health ($N = 24$ patients) under Human Research Ethics Committee approval (HREC 2017.336 and HREC/14/Austin/425). For HREC/14/Austin/425, patients consented to their tissue (stored or future) being used in translational research. A consent waiver was granted by the HREC as part of 2017.336 for retrospective use of tissues for research purposes.

Sections had previously been staged using standard pathology diagnostics (H&E and IHC for CK 5/6 and ER where appropriate). Sections

(formalin-fixed, paraffin-embedded) were either mounted on the nanoslide or on glass slides (SuperFrost Plus, Thermo Scientific) for H&E and IHC for antibody-based detection of CK 5/6 (1:100, clone D5/16 B4, Dako) or ER (cat. 790-4325, clone SP1, ~1 μg ml^{-1}, Ventana). For nanoslide processing, sections were dewaxed in Histolene and coverslipped for permanent storage and imaging. Scoring of nanoslide was performed, alongside H&E morphological assessment and analysis of CK 5/6 and ER staining. Nanoslide scoring was assessed as percentage of positive epithelial/tumour cells.

Digital image analysis

MMTV-PyMT model. Digital analysis based on the image pixel hue, saturation and lightness (HSL) associated with cancer cells for both nanoslide and Ki67 was carried out for the PyMT mouse model. Regions of cancer positivity were identified from the corresponding image pixel HSL colour space values. To establish an HSL range for cancer cells on nanoslide and Ki67, slides were compared to the ground truth standard for the PyMT model from the pathology annotation of the adjacent H&E breast tissue sections conducted on the high-resolution images (200× magnification). This follows similar protocols established in the literature for segmentation of Ki67 images[30]. Based on the measured values (of HSL), the mean values for the relevant colour channels for Ki67 and nanoslide could be calculated as shown in Supplementary Table 2. For the data presented, a maximum threshold of 15% (maximum colour difference) was set around the mean value for the mouse tissue, within this range cells were counted as 'positive'. The colour variation of cancer positive cells in the IHC staining occurs due to the heterogeneity in the expression of Ki67 while on nanoslide it is due to variations in the local sample dielectric constant. Across the small animal model we have studied, the measured values (of HSL) corresponding to cancer cells in Ki67 and nanoslide are almost entirely confined to the cancer specific regions (or those that are pre-cancer lesions in this model—hyperplasia). For both Ki67 and nanoslide outside the regions of cancer positivity there were only scattered areas of isolated positive pixels as well as a small number of single-pixel-width lines of positive pixels (the latter typically occurred at the very edges of the tissue sections). In other types of tissue, the colour was observed to be sufficiently different that these could not be mistaken for cancers by either a pathologist or by digital image analysis. All digital image analysis was performed using ImageJ (version 1.8) software, GIMP (version 2.10.20) and MATLAB (version R2020b).

In order to characterize the 'intensity' of Ki67 and nanoslide, we determined the absolute difference between the image pixel HSL colour space values (H, S, L) and the mean values for positive cells (H_M, S_M, L_M; equation (9)). Note, however, that this does not necessarily reflect the contrast perceived by the human eye when examining these samples under the microscope.

$$\chi = \sqrt{(H - H_M)^2 + (S - S_M)^2 + (L - L_M)^2} \quad (9)$$

Retrospective breast cancer patient cohort. Just as for the MMTV-PyMT model, digital analysis based on the image pixel HSL values associated with cancer cells for CK 5/6, ER and nanoslide was carried out for the DCIS retrospective cohort. Regions of cancer positivity were identified from the corresponding image pixel HSL colour space values. Based on the measured values (of HSL) the mean values for the relevant colour channels for CK 5/6, ER and nanoslide could be calculated as shown in Supplementary Table 3. A threshold of 8% (maximum colour difference) was set around the mean value for the patient tissues and within this range cells were counted as 'positive'. The colour variation of cancer positive cells in the IHC staining occurs due to the heterogeneity in the expression of CK 5/6 and ER. Across the patients who participated in this study, the measured values (of HSL) corresponding to cancer cells in CK 5/6, ER and nanoslide are typically confined to the cancer specific regions. Similar to the MMTV-PyMT model, there were only scattered areas of positive pixels (for example, single pixels or single-pixel-width lines) outside regions identified as cancerous by the pathologist). In other types of tissue, the colour is sufficiently different that these other tissues could not be mistaken for cancers by a pathologist or by digital image analysis.

For both the mice and patient samples, some colour variation will occur in nanoslide owing to different slices/regions of the individual cells being present within the characteristic SPP decay length. We have observed that this variation in colour (according to the HSL colour space values) is typically small compared to the differences in colour between cancer cells and other non-cancerous tissue.

Sensitivity of nanoslide

Conservatively, within the visible range, it is possible to detect a shift of 1 nm in the SPP resonance peaks using a spectrometer (HR4000, 200–1,100 nm, Ocean Optics Inc.). For the devices presented in this paper this would equate to a change in refractive index (ΔRI) of 2.3×10^{-3}. Further, although there is a lack of consensus in the published literature on the sensitivity of the human eye, based on our previous work in characterizing nanoslide we can make a conservative estimate of the change in dielectric constant that would be visible to the pathologist 'by eye' under the microscope. Changes in RI of >0.05 in the sample result in a distinct colour change that can be readily observed by the human eye under the microscope. This is based on a series of optical calibration experiments that have been performed using test samples of known RI[21].

Effect of variations in sample height

Histology samples produced by microtome typically exhibit variations in sample height of around 1% of the total thickness[48]. However, in general, extraordinary optical contrast will not be sensitive to these variations as the tissue sections are much thicker than the characteristic decay length of the SPP electromagnetic field (240 nm for the devices presented here). To experimentally demonstrate this, we show images (Extended Data Fig. 10) from adjacent tissue sections with differences in thickness of 1 μm (substantially larger than the typical variations due to microtome) that show that the results are insensitive to the thickness variation. The transmission electron microscopy (TEM) samples presented (Extended Data Fig. 9) are produced by ultramicrotome and have a total thickness which is less than the SPP decay length, yet there are no noticeable effects for a set thickness (70 nm or 200 nm) due to sample height variations. We conclude that for the samples presented in this manuscript, artefacts due to non-uniformity in height are not observed. However, it is important to note that in general for sample thicknesses of the order of a few hundred nanometres or less these effects need to be considered.

Adherence of biological tissues

A critical aspect of the devices presented here are that the surface is flat and enables good adherence of the tissue sections. The appearance of any 'gaps' between the tissue and the surface of the devices will result in colour change (if the gap is <200 nm) or, much more likely, a loss in contrast. Tissues with a high fat content, such as breast tissue in particular, do not adhere well to glass. The presence of any gaps, as well as causing a degradation in performance of the plasmonics, also leads to issues with IHC and H&E staining (that is, pooling of the dye under the tissue). A widely used solution to this problem is to apply a positive charge to the surface of the microscope slides, which ensures good contact between the slide and the tissue[49]. Here we adopt a similar approach. As part of the research in developing our devices, we developed a protocol of capping the surface with nanometre-thick layers of either SiO_2 or hydrogen silsesquioxane (HSQ). This has a threefold benefit: (1) the resulting surface is perfectly flat and 'glass-like'; (2) a polar interface is presented to the tissue and, much like the commercially available

charged slides, this has the effect of ensuring excellent adherence and eliminating gaps; and (3) the protected surface is extremely robust and the devices can be aggressively cleaned and placed in the autoclave at temperatures >70 °C without any detectable loss of performance.

Tissue classification

To quantify the performance and correlation between nanoslide and Ki67 staining, high-resolution imaging data were collected from the slides. A total of 64 regions were examined across the 24 tissue sections. Following established protocols[30,50], tissue was classified as true positive (TP), true negative (TN), false positive (FP) and false negative (FN) (see Supplementary Table 4). Two key pieces of information were used for tissue classification. The first was pathology annotation. When a cancer containing region has been identified, high-resolution H&E stained slides were used to identify the stage of the cancer and the margins. A morphological assessment of the tissues formed the 'ground truth' for the analysis presented in Extended Data Fig. 6. The second piece of information came from the image pixel HSL colour space values, which were compared against the reference values from the training data.

To determine the performance of the nanoslide throughout tumorigenesis, regions containing normal, hyperplasia, MIN (as a surrogate for DCIS) and invasive neoplastic breast tissue were independently analysed for both nanoslide and Ki67 staining. Representative images of each type of region and resulting tissue classification are shown in Extended Data Fig. 6a. The bright-field images, as they appear directly under the microscope, can be observed in Supplementary Video 1. Confirming the results of the large field-of-view positivity analysis (Extended Data Fig. 4, bottom row), neoplastic cells in pre-invasive and invasive neoplastic tissues could be distinguished from surrounding cells in the same tissue and epithelial cells from normal (non-cancer) tissues via a colorimetric differential interaction as a result of either staining (Ki67, brown colour) or as a result of variations in the local dielectric constant (nanoslide, blue colour). As seen from Extended Data Figs. 4 and 6, and Supplementary Figs. 3 and 4 (Supplementary Fig. 4 shows a false positive test using healthy tissue), adipose tissue and other types of non-cancerous cells observed across the slides typically have a characteristically different colour on both the nanoslide and Ki67, supporting this association. It should be noted however that in this MMTV-PyMT mouse model, neither Ki67 nor nanoslide provided a clear distinction between the hyperplasia and MIN states (although nanoslide had the larger difference). In addition to the percentage of positive cancer cells we also quantified the 'intensity' of the colorimetric change on the basis of the absolute difference compared to the mean HSL colour space values for both nanoslide and Ki67 (Extended Data Fig. 6b). The Dice coefficients (DSC) were calculated according to equation (10) using the classification scheme summarized in Supplementary Table 4.

$$\mathrm{DSC} = \frac{2\mathrm{TP}}{2\mathrm{TP} + \mathrm{FP} + \mathrm{FN}} \tag{10}$$

Statistics

Mouse model. The aim with the C57 BL/6 MMTV-PyMT model was to determine if we could differentiate normal epithelial cells from cancer cells in a clearly defined disease state at the earliest stages of tumorigenesis. This model and sample size were chosen on the basis of previous biomarker studies in the PyMT model, where three tissues representing each pathological stage were determined to be sufficient to discriminate stages using Ki67[26]. The present study incorporated 24 tissues taken from 6 mice, each with varied pathologies. After pathology classification, this yielded sample sizes of 4, 5, 4 and 2 (nanoslide) and 3, 5, 6 and 3 (Ki67) for normal, hyperplasia, MIN and invasive cancer, respectively. A two-tailed unpaired *t*-test was used to compare data between each of the two groups at a 0.05 significance level. A *P* value was used to evaluate the correlation between Ki67 and nanoslide.

DCIS patient cohort. A total of 24 patients were incorporated into this study. Sample sizes of 6, 6, 6 and 6 are obtained from 4 groups (normal breast, UDH, DCIS and invasive breast cancer). A post hoc power analysis was conducted. A single factor ANOVA analysis was carried out for the percentage of cells positively identified. A Tukey–Kramer (pairwise) multiple comparison test was used to confirm the significance of differences between groups for the number of subjects. All data were analysed using GraphPad Prism software (v.9.0.2).

Visualization of ultra-thin sections

In Extended Data Fig. 9 we present the results of applying histoplasomics to imaging TEM sections of optic nerve tissue. These sections can typically only be viewed using an electron microscope (Supplementary Fig. 5) and are too thin to characterize using either staining or conventional optical microscopy techniques (Supplementary Fig. 6). We also note that although our method requires a white light source and so certain high-resolution techniques (for example, confocal) are not compatible with colorimetric histology, it is still possible to combine this form of histology with data collection in reflection mode. For example, fluorescence microscopy in reflection mode could be combined with histoplasmonics.

Reporting summary

Further information on research design is available in the Nature Research Reporting Summary linked to this paper.

Data availability

All data sets are included in this article and its Supplementary Information files. Pathology scoring for Figs. 3d and 4e was conducted on the basis of visual inspection of the slides by expert breast cancer pathologists using an Olympus BX51 optical microscope. Histology images used for this study are available in figshare with the identifier https://doi.org/10.6084/m9.figshare.14897697.v2. Source data are provided with this paper.

35. Balaur, E., Sadatnajafi, C. & Abbey, B. Large-scale fabrication of optically active plasmonic arrays via displacement Talbot lithography. *J. Phys. Conf. Ser.* **1455**, 012005 (2020).
36. Balaur, E., Sadatnajafi, C., Kou, S. S., Lin, J. & Abbey, B. Continuously tunable, polarization controlled, colour palette produced from nanoscale plasmonic pixels. *Sci. Rep.* **6**, 28062 (2016).
37. Balaur, E., Sadatnajafi, C., Langley, D. & Abbey, B. Optimisation of polarization controlled colour tuning using nanoscale cross-shaped apertures in silver films. *Proc. SPIE* **10013**, 100132F (2016).
38. Namatsu, H. et al. Three-dimensional siloxane resist for the formation of nanopatterns with minimum linewidth fluctuations. *J. Vac. Sci. Technol. B* **16**, 69 (1998).
39. Giannuzzi, L. A. *Introduction to Focused Ion Beams* 1st edn (Springer US, 2005).
40. Jung, L. S., Campbell, C. T., Chinowsky, T. M., Mar, M. N. & Yee, S. S., Quantitative interpretation of the response of surface plasmon resonance sensors to adsorbed films. *Langmuir* **14**, 5636–5648 (1998).
41. Maier, S. A. *Plasmonics: Fundamentals and Applications* (Springer US, 2007).
42. Balaur, E. et al. Plasmon-induced enhancement of ptychographic phase microscopy via sub-surface nanoaperture arrays. *Nat. Photon.* **15**, 222–229 (2021).
43. Sadatnajafi, C., Balaur, E. & Abbey, B. Bimodal plasmonic color filters enable direct optical imaging of ion implantation in thin films. *Adv. Funct. Mater.* https://doi.org/10.1002/adfm.202009419 (2021).
44. Simmons, D. M. & Swanson, L. W. Comparing histological data from different brains: sources of error and strategies for minimizing them. *Brain Res. Rev.* **60**, 349–367 (2009).
45. Niazi, M. K. K. et al. Relationship between the Ki67 index and its area based approximation in breast cancer. *BMC Cancer* **18**, 867 (2018).
46. Davie, S. A. et al. Effects of FVB/NJ and C57Bl/6J strain backgrounds on mammary tumor phenotype in inducible nitric oxide synthase deficient mice. *Transgenic Res.* **16**, 193–201 (2007).
47. Orian, J. M. et al. Insertional mutagenesis inducing hypomyelination in transgenic mice. *J. Neurosci. Res.* **39**, 604–612 (1994).
48. Matenaers, C., Popper, B., Rieger, A., Wanke, R. & Blutke, A. Practicable methods for histological section thickness measurement in quantitative stereological analyses. *PLoS ONE* **13**, e0192879 (2018).
49. Thurby, C., White, M. R., Simutis, F., Gillham, S. & Slinker, D. An improved method of tissue adhesion on glass microslides for immunohistochemical evaluation by the use of selected tissues from the dog and monkey. *J. Histotechnol.* **32**, 198–201 (2009).

50. Cruz-Roa, A. et al. Accurate and reproducible invasive breast cancer detection in whole-slide images: a deep learning approach for quantifying tumor extent. *Sci. Rep.* **7**, 46450 (2017).

Acknowledgements B.A., E.B. and K.A.N. acknowledge the support of the Australian Research Council through the Centre of Excellence in Advanced Molecular Imaging (CE140100011). Fellowship funding from the Victorian Cancer Agency and grant funding from the National Breast Cancer Foundation NBCF (IIRS-21-069) is acknowledged by B.S.P. Funding from the National Breast Cancer Foundation (NBCF Prac. 16-006) and Sydney Breast Cancer Foundation is acknowledged by S.O'T. B.A. acknowledges support from the La Trobe Biomedical and Environmental Sensor Technology (BEST) Research Centre. The authors gratefully acknowledge X. Li from the La Trobe Statistics Consultancy Platform for help and advice with the statistical analysis of the data. This work was performed in part at the Melbourne Centre for Nanofabrication (MCN) in the Victorian Node of the Australian National Fabrication Facility (ANFF).

Author contributions E.B. carried out the research, performed the measurements, analysed the data and generated the figures for the manuscript. E.B., B.S.P. and B.A. conceived the idea and are responsible for the conceptual design of the study. E.B. and B.A. jointly developed the original concept for 'nanoslide' and 'histoplasmonics'. B.S.P. was responsible for design and management of cancer histological studies. B.M. and B.Y. sourced patient samples and assisted with diagnostic sample identification for study. C.S. assisted with experiments. E.H., B.S.P. and A.S. prepared the biological samples and microtome slices. J.O. prepared the optic nerve samples. S.O'T. and B.S.P. performed the pathology scoring and, along with K.H., prepared patient samples. B.A. directed the project. K.A.N. discussed the results and analysis. B.A., B.S.P. and E.B. wrote the paper. All authors discussed the results and contributed to the manuscript.

Competing interests The authors declare no competing interests.

Additional information

Supplementary information The online version contains supplementary material available at https://doi.org/10.1038/s41586-021-03835-2.

Correspondence and requests for materials should be addressed to Belinda S. Parker or Brian Abbey.

Peer review information *Nature* thanks Roberto Salgado and the other, anonymous, reviewer(s) for their contribution to the peer review of this work.

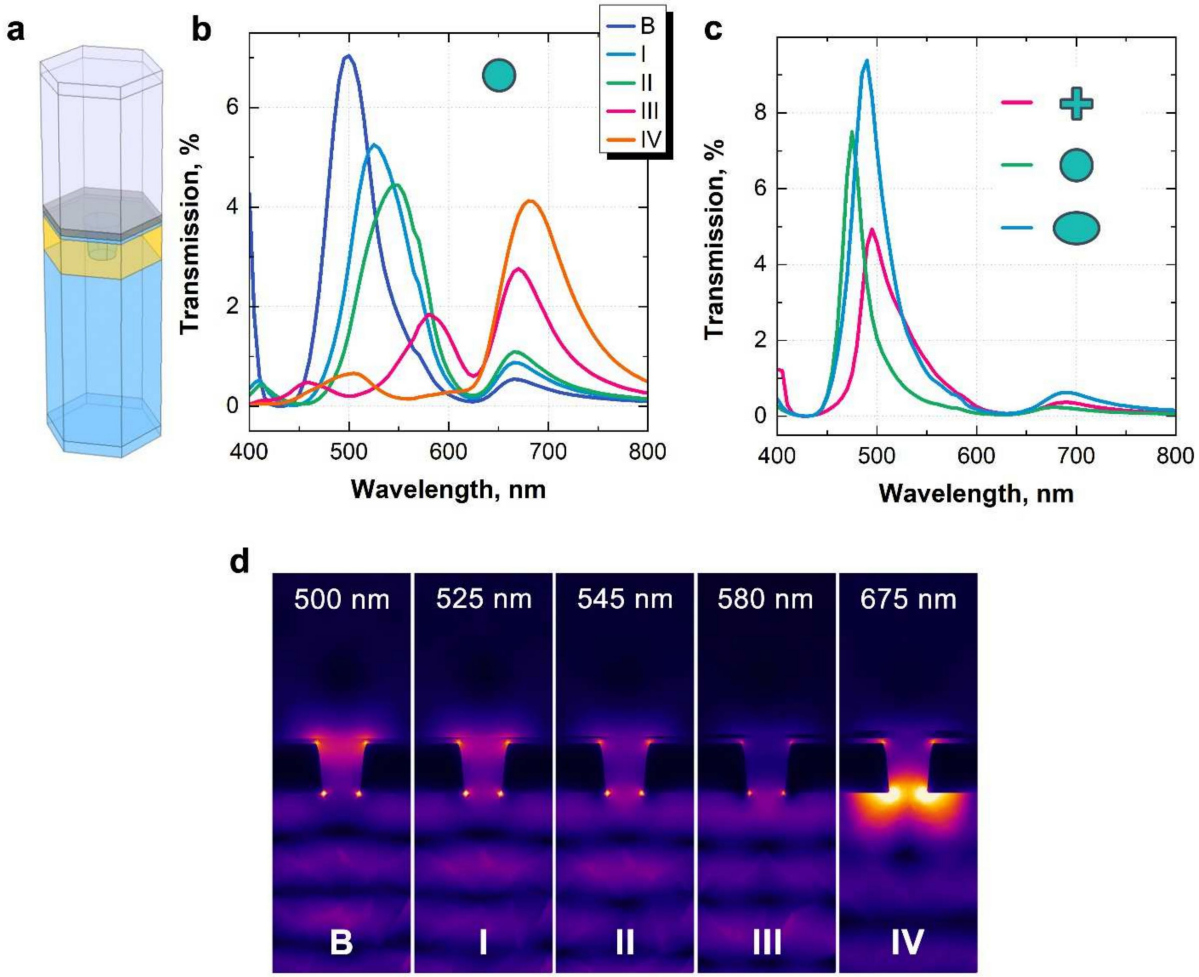

Extended Data Fig. 1 | Finite element methods (FEM) optical transmission simulations. a, FEM model of a section of the nanoslide showing the glass substrate (dark blue), nanoaperture in the metallic film, the capping layer, and air (light blue) constructed in the COMSOL Multiphysics software program. Simulated transmission spectra from each of the four lines (I-IV) which make up the chevron sample (see Fig. 2) and the background (B) spectrum generated using **b**, FEM model of the device for circular apertures (diameter = 160 nm). **c**, Shows the simulated background spectrum (no sample) for the crosses (arm length = 160 nm), ellipse (major axis = 210 nm, minor axis = 160 nm), and circular apertures. The peaks represent the plasmon resonances that occur within the active layer of the device. **d**, Example FEM simulations of a cross section of the electric field generated by a single circular nanoaperture at the peak resonant wavelength of the spectra shown in **b**.

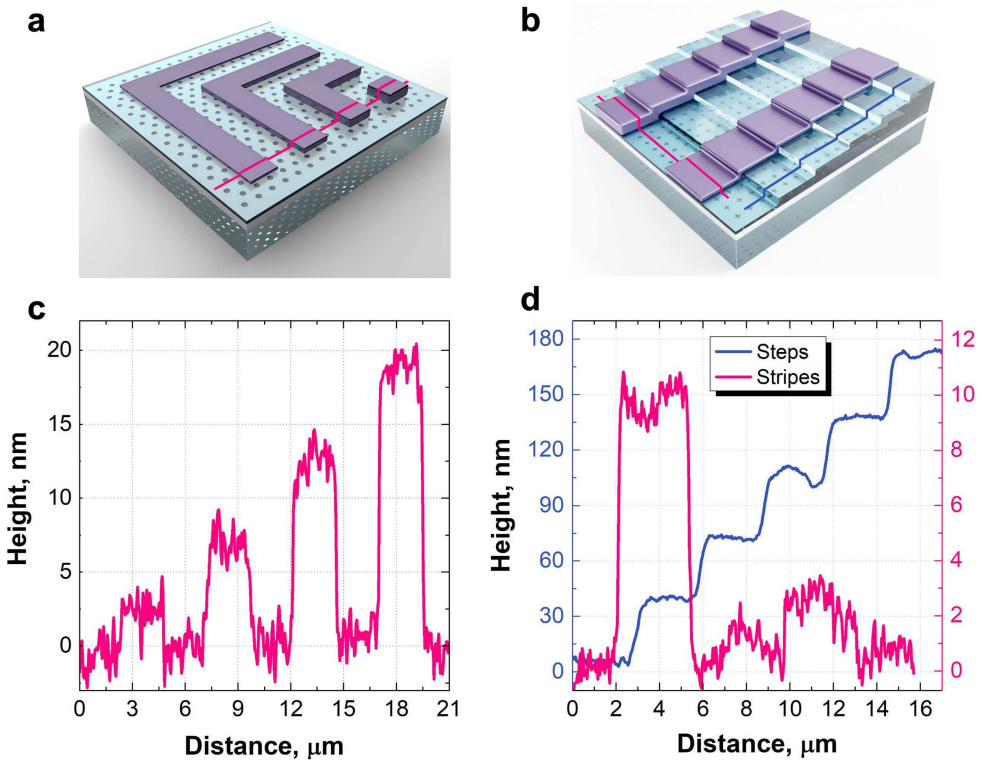

Extended Data Fig. 2 | AFM line-scan height profiles of the fabricated samples. a, Schematics of the chevron structure and **b**, the 'staircase' sample. **c**, The AFM line-scan height profile of the chevron structure sample, the thinnest sample stripe is 3 ± 1 nm. **d**, The AFM line-scan height profile across the steps and stripes respectively of the 'staircase' sample.

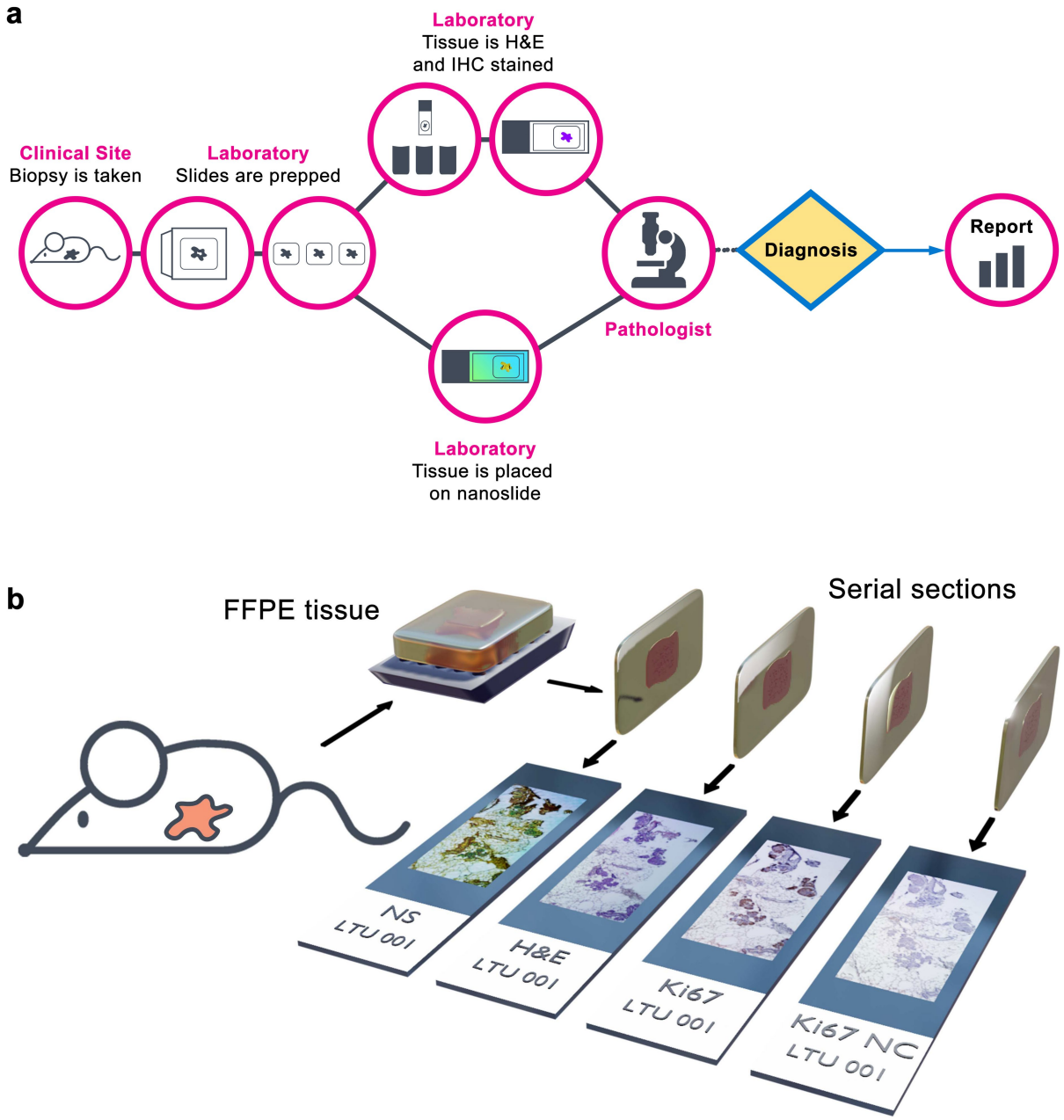

Extended Data Fig. 3 | Pathology workflow for small-animal study and schematic showing serial sections used. a, Pathology workflow for small-animal, MMTV-PyMT mouse model study. **b**, Schematic showing how serial sections were taken to enable a direct comparison of nanoslide, H&E, and Ki67.

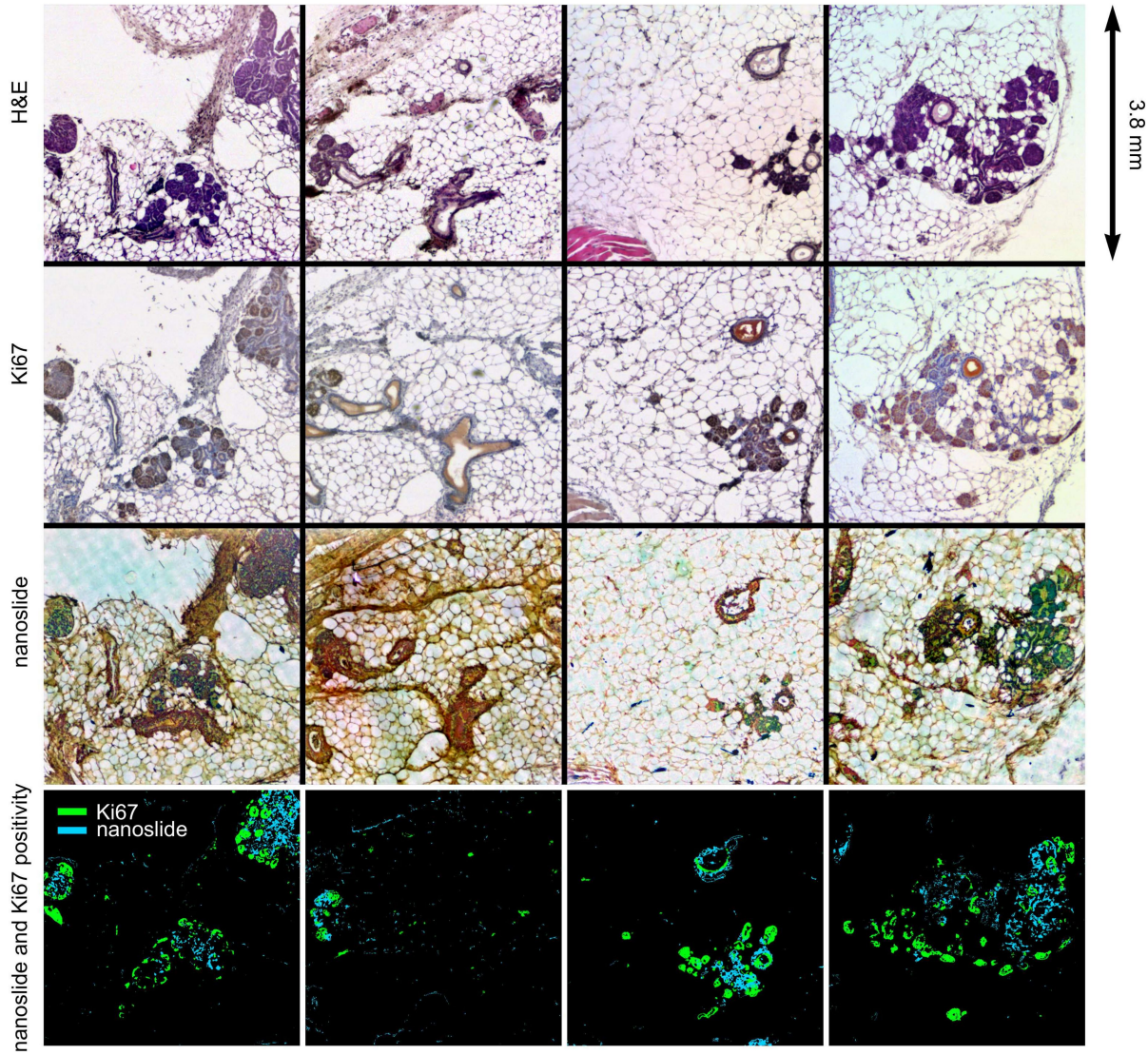

Extended Data Fig. 4 | Large field-of-view example images from H&E, Ki67, and nanoslide. The Ki67 and nanoslide positive areas are overlaid. Large-field-of-view (3.8 × 3.8 mm^2) areas of tissue stained with H&E and Ki67 compared to the results obtained directly on nanoslide. The areas of positivity of both nanoslide (light blue) and Ki67 (bright green) were identified based on their respective HSL colour space values for example, ref. [32] (also see Methods).

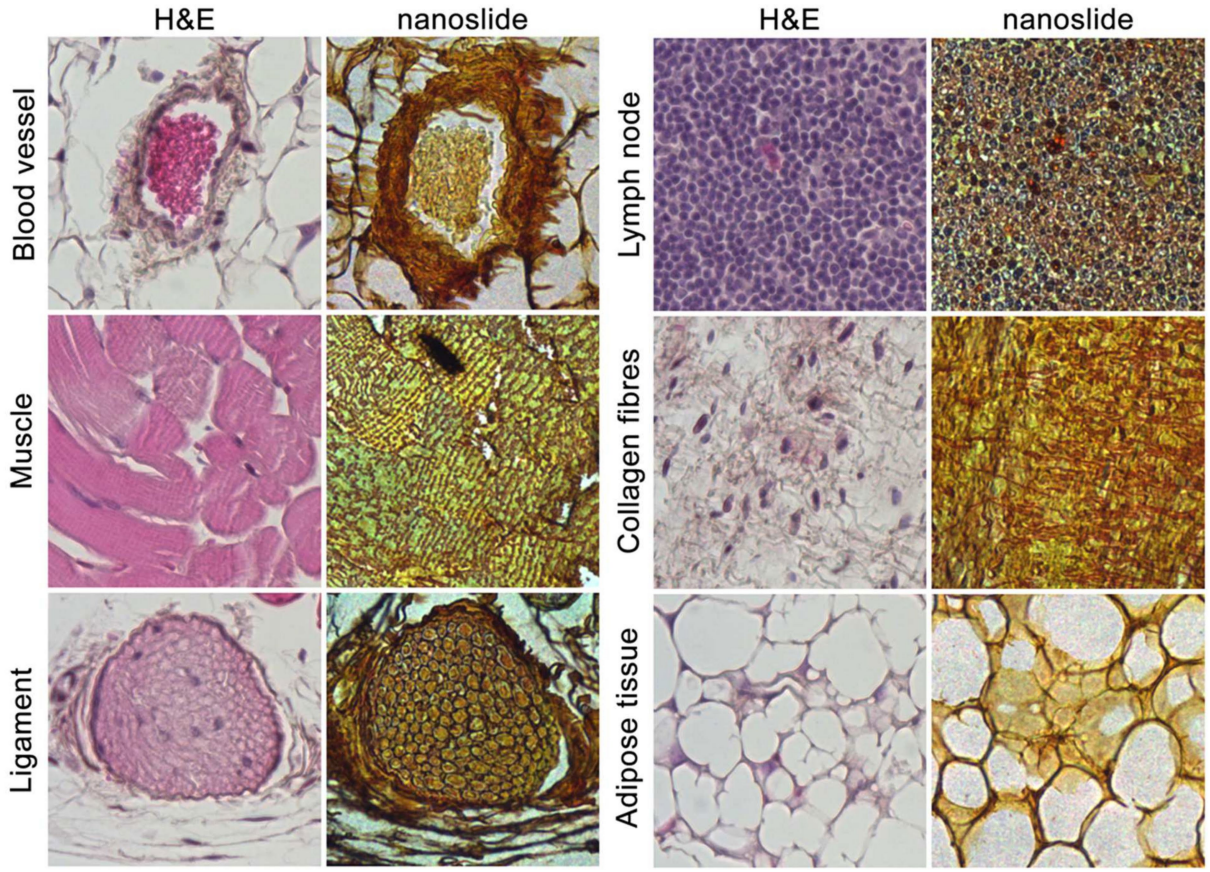

Extended Data Fig. 5 | Comparison of histoplasmonics to H&E staining of different tissues. Bright-field optical images: H&E stained images and histoplasmonic images. Tissue slices were placed on the slides in a sequential manner.

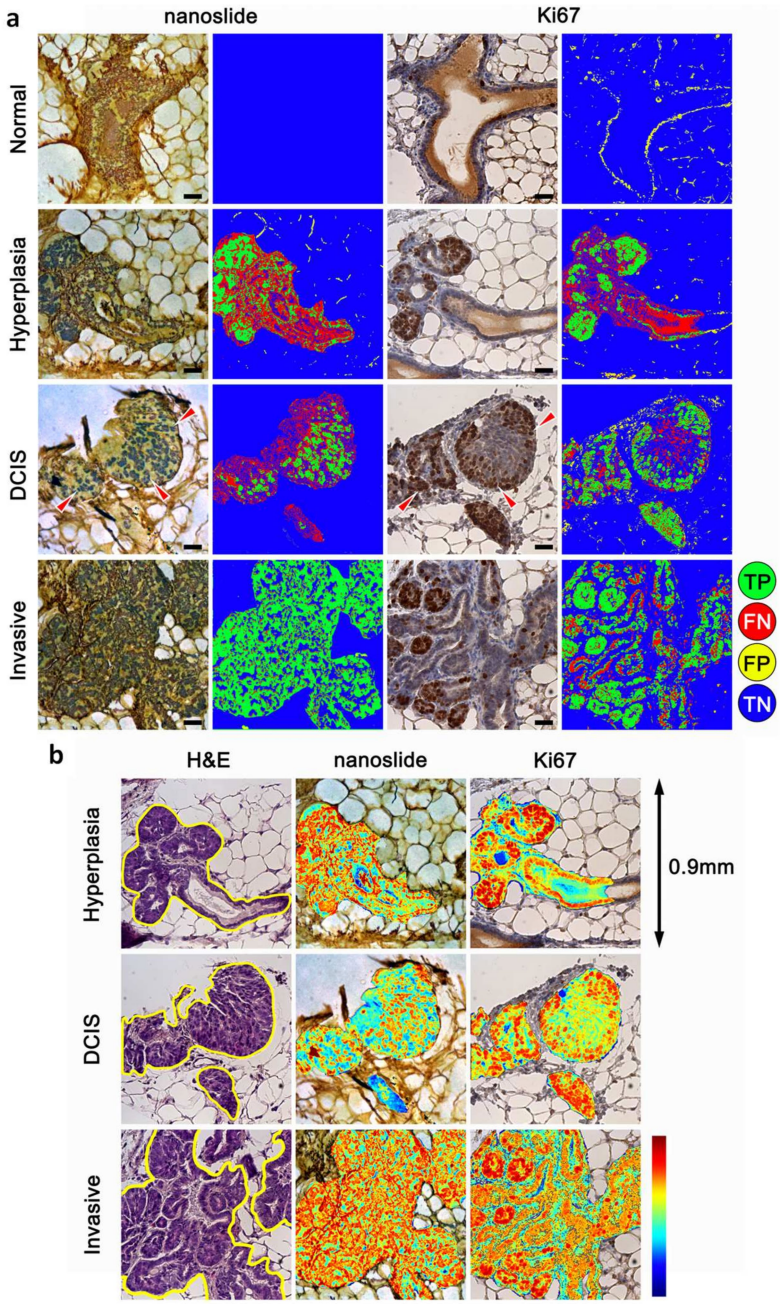

Extended Data Fig. 6 | Colorimetric analysis and pathology assessment of mouse data. a, Histology images (200× magnification) were sub-categorized into four different stages for both nanoslide (1st column) and Ki67 (3rd column). The HSL image pixel colour space values were compared against ground truth pathology annotations and classified as True Positive (TP - green), False Negative (FN - red), False Positive (FP - yellow), and True Negative (TN - blue). The white space in the Ki67 image in the top row is an area where no stain adhered. Scale bars = 15 µm. **b**, H&E images for neoplastic regions –yellow outline (1st column), nanoslide intensity (2nd column), and Ki67 (3rd column) positivity.

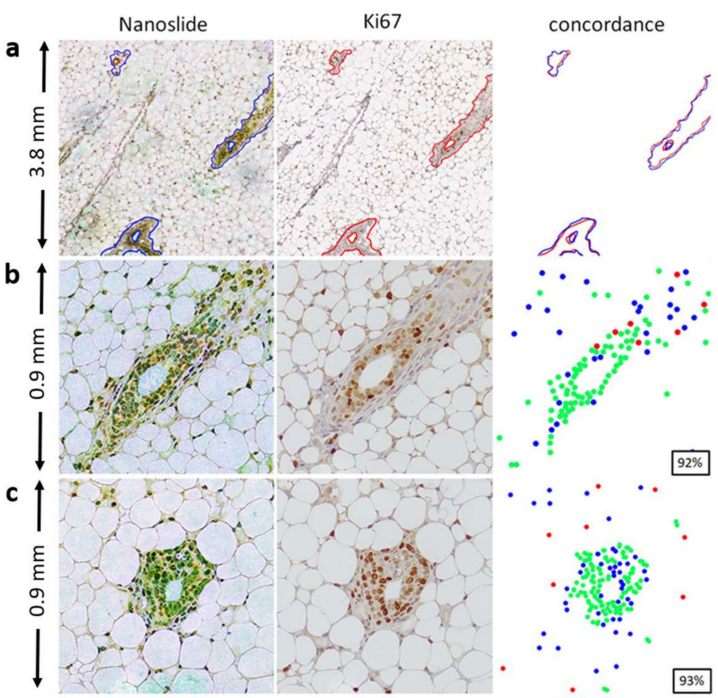

Extended Data Fig. 7 | Cell counting Ki67 vs nanoslide using brightfield microscopy. Example histoplasmonic images of 1 µm thick sequential cancerous breast tissues (PyMT mice). **a**, Low magnification (× 100) images. Left: contouring of cancerous regions on Nanoslide. Middle: contouring of the same cancerous regions using Ki67. Right: the contours for Nanoslide (blue) is overlapped with the contour for Ki67 (red). **b**, High magnification (× 200) images. Left: Nanoslide image of MIN region; Middle: Ki67 image of the same region. Right: Overlap of positive cells on Nanoslide and MIN (92% concordance). **c**, High magnification (×200) images. Left: Nanoslide image of MIN region; Middle: Ki67 image of the same region. Right: Overlap of positive cells on Nanoslide and MIN (93% concordance).

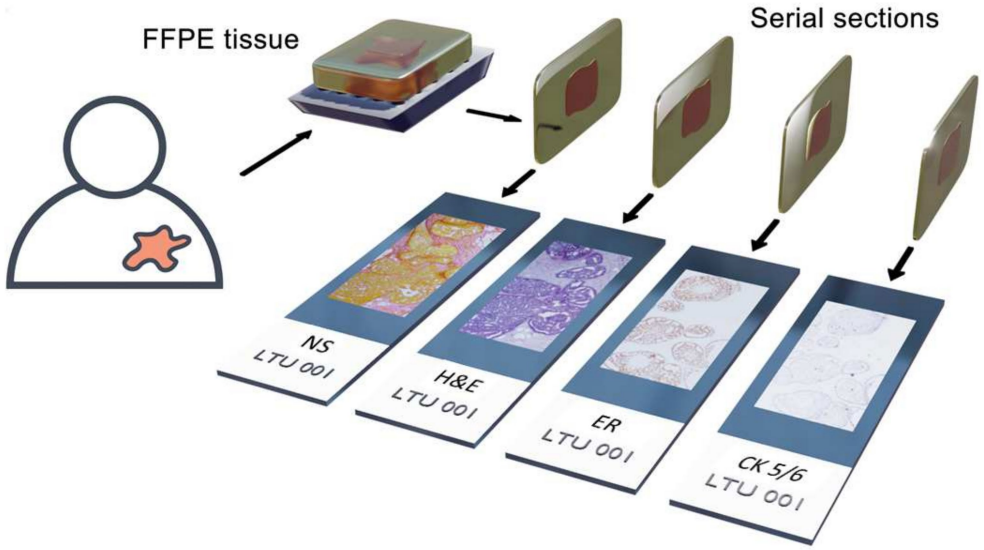

Extended Data Fig. 8 | Schematic showing serial sections used for DCIS breast cancer patient study. Schematic showing how serial sections were taken to enable a direct comparison of nanoslide, H&E, ER, and CK 5/6 for human tissue.

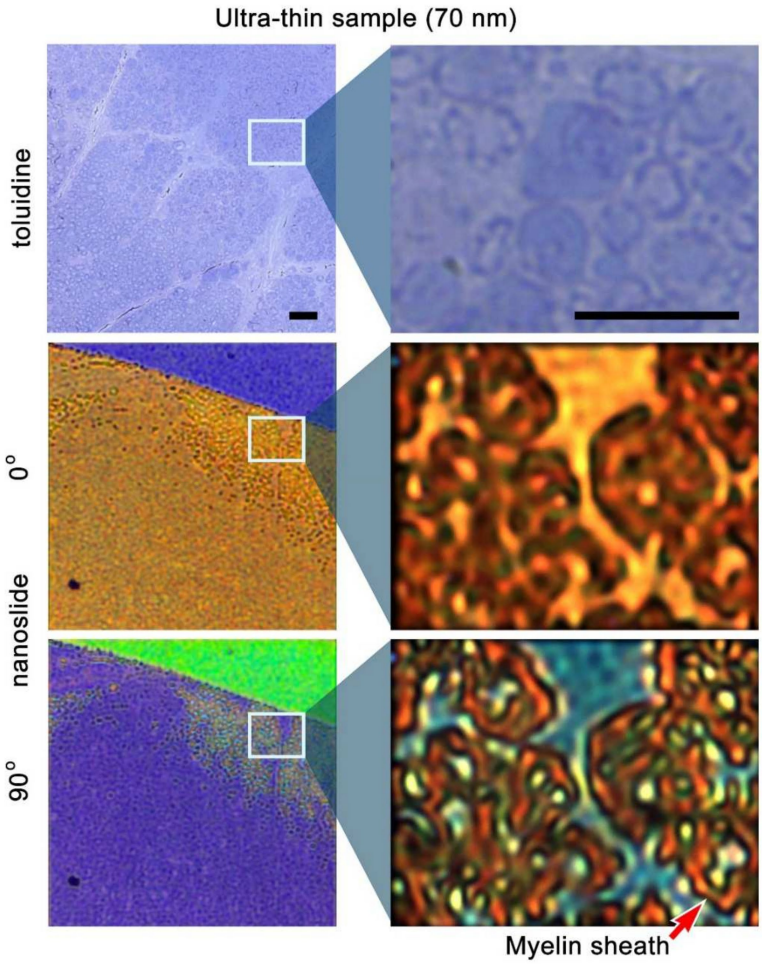

Extended Data Fig. 9 | Bright-field microscopy of 70 nm thick TEM optic nerve tissue sections imaged using toluidine staining and with histoplasmonics. Top: Bright-field optical image of toluidine stained 70 nm thick optic nerve sections. Nanoslide results: middle – at 0° incident polarization, bottom – at 90° incident polarization reveals axons, glia and the myelin sheath as different colours. The black scale bar in both the left and right column images is 5 µm.

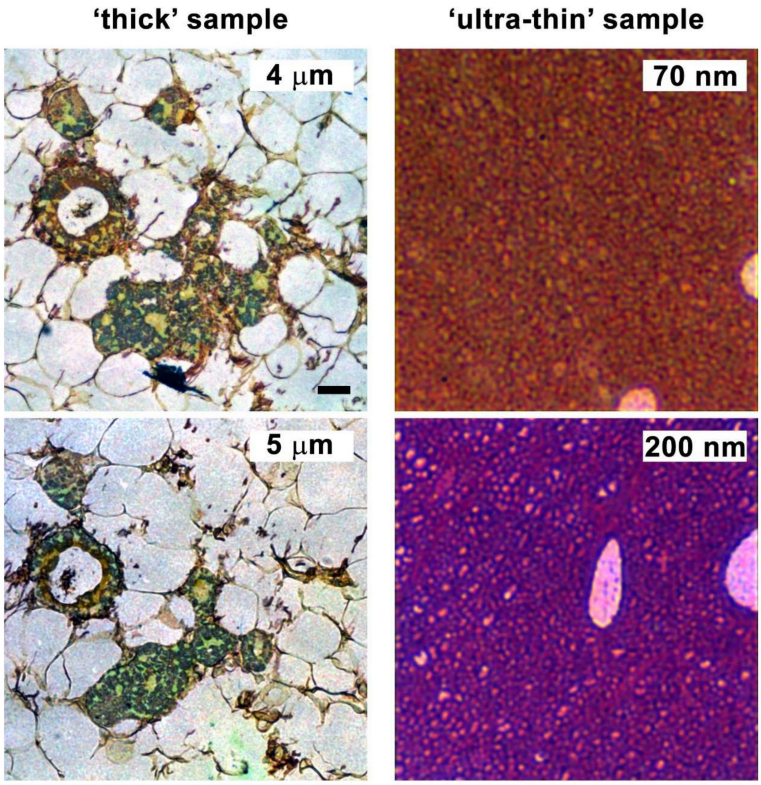

Extended Data Fig. 10 | Bright-field microscopy of tissues of different thicknesses. Left: Histoplasmonic images of cancerous breast tissues (PyMT mice) sectioned at 4 and 5 μm slice thickness showing almost no difference in colour contrast. Right: Bright-field optical images of optic nerve sections sectioned at 70 and 200 nm thickness showing dramatic difference in colour contrast. The scale bar is 15 μm.

Extended Data Table 1 | Comparison of key label-free techniques for histology

Technique Category	Key features of existing label-free method	Advantages/disadvantages of histoplasmonics
Photoacoustic and UV microscopy[15,16]	• Generates histology-like images. • Fast-rapid, label free imaging. • Suitable for intraoperative pathology. • Enables coarse (40-50 µm) depth resolution. • Requires specialized UV-PAM (photoacoustic mode system) equipment. • Does not fit into standard pathology workflows. • Specialized software required for data collection and analysis.	• Generates chromatic histology-like images. • Fast-rapid, label free imaging. • Suitable for intraoperative pathology. • Uses a standard brightfield microscope (non-specialized). • Fits into standard pathology workflows. No changes to sample preparation or mounting. • No specialized software required; diagnosis made directly at microscope. • Does not enable any depth resolution.
Quantitative mass spectroscopy and bioanalytical imaging[17]	• Measures chromatographic peak areas. • Does not provide any information on sample morphology which can aid diagnosis. • Provides molecular information from specific cell types within tissue sections. • Requires access to mass-spectrometer which may not be readily available. • Suitable for intraoperative pathology. • Requires specialized software and training for quantification.	• Generates chromatic histology-like images. • Provides images of sample morphology which can aid diagnosis. • Cannot quantify protein amounts in sample mixtures. • Uses a standard brightfield microscope (non-specialized). • Suitable for intraoperative pathology. • No specialized software required; diagnosis made directly at microscope.
Stimulated Raman scattering microscopy[18,19]	• Probes the intrinsic vibrational frequencies of chemical bonds. • Generates label-free histology like images with sensitivity to DNA. • Not suitable for intraoperative pathology. • Time-consuming and restricted to comparatively small sample areas. • Can be applied to live samples. • Does not fit into pathology workflows. • Requires highly specialized equipment.	• Generates chromatic histology-like images. • Does not provide molecular contrast. • Suitable for intraoperative pathology. • Provides rapid diagnosis on whole tissue sections (> cm in size). • Unproven for live samples (though technically feasible). • Fits into standard pathology workflows. • Uses a standard brightfield microscope.
Quantitative phase imaging[20]	• Generates wide-field label-free phase contrast images. • Quantitative analysis of tissue density. • Potentially suitable for intraoperative pathology. • Limited to samples within a certain thickness range (to avoid phase wrapping). • Requires specialized software and training for analysis of phase images.	• Generates chromatic histology-like images. • Unproven for quantitative analysis of tissue density. • Suitable for intraoperative pathology. • Applicable to optically transparent samples of any thickness, though below ~200 nm will be sensitive to height variations. • No specialized software required; diagnosis made directly at microscope.

Comparison of the features, advantages and disadvantages of histoplasmonics versus other key label-free tissue imaging techniques.

nature research

Corresponding author(s): Brian Abbey, Belinda Parker

Last updated by author(s): 2021-6-23

Reporting Summary

Nature Research wishes to improve the reproducibility of the work that we publish. This form provides structure for consistency and transparency in reporting. For further information on Nature Research policies, see our Editorial Policies and the Editorial Policy Checklist.

Please do not complete any field with "not applicable" or n/a. Refer to the help text for what text to use if an item is not relevant to your study.
For final submission: please carefully check your responses for accuracy; you will not be able to make changes later.

Statistics

For all statistical analyses, confirm that the following items are present in the figure legend, table legend, main text, or Methods section.

n/a	Confirmed	
☐	☒	The exact sample size (*n*) for each experimental group/condition, given as a discrete number and unit of measurement
☐	☒	A statement on whether measurements were taken from distinct samples or whether the same sample was measured repeatedly
☐	☒	The statistical test(s) used AND whether they are one- or two-sided *Only common tests should be described solely by name; describe more complex techniques in the Methods section.*
☒	☐	A description of all covariates tested
☒	☐	A description of any assumptions or corrections, such as tests of normality and adjustment for multiple comparisons
☐	☒	A full description of the statistical parameters including central tendency (e.g. means) or other basic estimates (e.g. regression coefficient) AND variation (e.g. standard deviation) or associated estimates of uncertainty (e.g. confidence intervals)
☐	☒	For null hypothesis testing, the test statistic (e.g. *F*, *t*, *r*) with confidence intervals, effect sizes, degrees of freedom and *P* value noted *Give P values as exact values whenever suitable.*
☒	☐	For Bayesian analysis, information on the choice of priors and Markov chain Monte Carlo settings
☒	☐	For hierarchical and complex designs, identification of the appropriate level for tests and full reporting of outcomes
☐	☒	Estimates of effect sizes (e.g. Cohen's *d*, Pearson's *r*), indicating how they were calculated

Our web collection on statistics for biologists contains articles on many of the points above.

Software and code

Policy information about availability of computer code

Data collection	No unpublished software utilised for initial data collection, initial paper records were later entered into generic excel spreadsheet
Data analysis	Device design software: COMSOL (version 5.6) Multiphysics package Mouse tissue data analysis software: GraphPad Prism software (v.9.0.2) was utilised for 2 tailed Mann Whitney/T tests and calculating Pearson correlation coefficients (r). Digital image analysis (e.g. quantifying Hue, Saturation, Lightness of the image pixel values) was performed using the following software: ImageJ (version 1.8) software, GIMP (version 2.10.20), and MATLAB (version R2020b) using the in-built functions. No custom code was developed especially for this study.

For manuscripts utilizing custom algorithms or software that are central to the research but not yet described in published literature, software must be made available to editors and reviewers. We strongly encourage code deposition in a community repository (e.g. GitHub). See the Nature Research guidelines for submitting code & software for further information.

Data

Policy information about availability of data

All manuscripts must include a data availability statement. This statement should provide the following information, where applicable:

- Accession codes, unique identifiers, or web links for publicly available datasets
- A list of figures that have associated raw data
- A description of any restrictions on data availability

All datasets are included in this article [and its supplementary information files]. Source data are applicable for Figs. 2c-d, 2f-g, Figs. 3a-e., Fig. 4e, Extended Data Fig. 1b-c, and Extended Data Fig. 2c-d and are available with the manuscript. Pathology scoring for Fig. 3d and Fig. was conducted based on visual inspection of the slides by expert breast cancer pathologists using an Olympus BX51 optical microscope. Histology images used for this study are available in figshare with the identifier [https://doi.org/10.6084/m9.figshare.14897697.v2]. Source data are provided with this paper.

Field-specific reporting

Please select the one below that is the best fit for your research. If you are not sure, read the appropriate sections before making your selection.

☒ Life sciences ☐ Behavioural & social sciences ☐ Ecological, evolutionary & environmental sciences

For a reference copy of the document with all sections, see nature.com/documents/nr-reporting-summary-flat.pdf

Life sciences study design

All studies must disclose on these points even when the disclosure is negative.

Sample size	Sample sizes for mouse models were chosen based on previous biomarker studies in the PyMT model, where 3 tissues representing each pathological stage was sufficient to discriminate stages using Ki67 (Duivenvoorden et al. 2018, ref[26]). This study incorporated 24 tissues taken from 6 mice, each with varied pathologies. For nanoslide sample sizes of 4, 5, 4, and 2 were obtained, for Ki67 sample sizes of 3, 5, 6, and 3 were obtained from four groups (Normal, hyperplasia, MIN, and invasive). Additional data was collected from healthy (pre-cancerous) tissue (6 samples for nanoslide and 5 samples for Ki67) and is included in the source data. Post-hoc analysis used a two-tailed unpaired t-test to compare data between each of the groups at a 0.05 significance level. A P value was used to evaluate the correlation between Ki67 and nanoslide. For patient participants, a post hoc power analysis was carried out assuming the "Minimum Detectable Difference" and "Standard Deviation". Here we assume the Minimum Detectable Difference range from 30 to 40, and Standard Deviation range from 3 to 10. In a single factor ANOVA study, sample sizes of 6, 6, 6, and 6 were obtained from the four groups whose means were compared. Comparing pathologist scores across four groups (Normal, DCIS, UDH, and invasive) a statistically significant difference was obtained ($F(3,21) = 320.608$, $p < 0.001$). The total sample of 24 subjects achieves 95% power to detect a difference of at least 30.00 using the Tukey-Kramer (Pairwise) multiple comparison test at a 0.0500 significance level. The common standard deviation within a group is assumed to be 3.00. A Bonferroni post hoc test revealed that the pairwise comparisons between the four groups are all significant with $p<0.05$.
Data exclusions	nil
Replication	We combined the data from different mouse experiments for presentation and comparison. Rather than replicating this study in the mouse system (given the limited variation within groups), we replicated the study in patient tissue.
Randomization	No randomization was required in this study as only retrospective tissues were used from patients that received no treatment prior to surgical resection. For mouse studies, the PyMT model develops spontaneous mammary tumor that progress through discrete stages of tumorigenesis. These mice are taken at set time points and scoring is assessed based on pathological stage across and within same tissues. For this reason, randomization in the mouse model is not applicable as scoring of different pathologies can be achieved across an identical tissue.
Blinding	Researchers were blinded to tissue pathological diagnostic information and disease staging in the mouse model and in patient tissues during nanoslide and IHC scoring, although the staging would have been obvious to the trained pathologist during independent scoring as H&E stained serial sections were used to guide regions of interest. However, scoring by independent pathologists/researchers was consistent validating that the approach had no inherent bias. Additionally, our digital image analysis provided in the manuscript confirmed the correlation between marker scoring. During statistical analysis of patient tissue scoring, data was separated into pathological groups and hence blinding was not possible.

Reporting for specific materials, systems and methods

We require information from authors about some types of materials, experimental systems and methods used in many studies. Here, indicate whether each material, system or method listed is relevant to your study. If you are not sure if a list item applies to your research, read the appropriate section before selecting a response.

Materials & experimental systems

n/a	Involved in the study
☐	☒ Antibodies
☒	☐ Eukaryotic cell lines
☒	☐ Palaeontology and archaeology
☐	☒ Animals and other organisms
☐	☒ Human research participants
☒	☐ Clinical data
☒	☐ Dual use research of concern

Methods

n/a	Involved in the study
☒	☐ ChIP-seq
☒	☐ Flow cytometry
☒	☐ MRI-based neuroimaging

Antibodies

Antibodies used

Anti-Ki67 (Abcam, Cat# ab15580, polyclonal, 1ug/mL final)
Anti-CK5/6 (Dako, Cat# M7237, Clone D5/16 B4, 1:100)
Anti-Estrogen Receptor (Ventana, Cat#790-4325, Clone SP1, ~1ug/mL)

Validation

The antibodies used in this study are widely used and validated, including knockout validated by the manufacturer. CK5/6 and ER staining was performed in a clinical laboratory under approval and to NATA standard. The well documented expression patterns in reduction mammoplasty tissue (normal breast epithelium) and in early breast cancer serves as a positive control, whereby other cells in the microenvironment were internal negative controls.

Animals and other organisms

Policy information about studies involving animals; ARRIVE guidelines recommended for reporting animal research

Laboratory animals

Mouse C57 BL/6, female, 8-12 weeks in age, sourced from WEHI, Parkville, Australia

Mice are housed in Allentown Individually Ventilated Caging, with a floor substrate of shredded corn cob. A commercially produced irradiated mouse diet is provided adlib and a rotated environmental enrichment program consisting of things such as, toilet rolls, tissues, shredded paper, cardboard boxes and cable ties is provided.

Mouse rooms are kept at a temperature of 21oC +/-1oC, with a relative humidity between 40 to 60%. There is a 14hr light and 10hr dark cycle programmed for the facility, with a 30 minute sunrise and 30 minute sunset at each end of the cycle.

Wild animals

No wild animals were used in the study

Field-collected samples

No field collected samples were used in the study

Ethics oversight

Ethics approved by the La Trobe Animal Ethics Committee

Note that full information on the approval of the study protocol must also be provided in the manuscript.

Human research participants

Policy information about studies involving human research participants

Population characteristics

Patients were identified from a prospectively maintained retrospective clinical database from electronic medical records. These patients were not selected based on any specific criteria other than their diagnostic breast pathology staging (normal, hyperplasia, DCIS, or invasive ductal carcinoma).

Recruitment

The samples used in this study were retrospective, taken previously at the time of biopsy or surgery in women undergoing post-screening biopsy or surgery. There was no selection bias as the only criteria for selection was their breast cancer stage.

Ethics oversight

Human Research Ethics Committee of Melbourne Health, RPAH and Austin Health. Normal breast, UDH, DCIS and invasive breast cancer sections were obtained from routine diagnostic samples taken at RMH and Austin health (N=24 patients) under Human Research Ethics Committee approval (HREC 2017.336 and HREC/14/Austin/425). For HREC/14/Austin/425, patients consented to their tissue (stored or future) to be used in translational research. A consent waiver was granted by the HREC as part of 2017.336 for retrospective use of tissues for research purposes.

Note that full information on the approval of the study protocol must also be provided in the manuscript.